University of Nebraska - Lincoln

## DigitalCommons@University of Nebraska - Lincoln

# Synthesis and Catalytic Activity of Nanostructured Cerium Oxide

Neil J. Lawrence
*University of Nebraska-Lincoln*, ohmmanipadmehum@gmail.com

Follow this and additional works at: https://digitalcommons.unl.edu/chemistrydiss

Part of the Environmental Chemistry Commons, Inorganic Chemistry Commons, and the Physical Chemistry Commons

# SYNTHESIS AND CATALYTIC ACTIVITY OF NANOSTRUCTURED CERIUM OXIDE

By

Neil Jamieson Lawrence

A THESIS

Presented to the Faculty of

The Graduate College of the University of Nebraska

In Partial Fulfillment of the Requirements

for The Degree of Master of Science

Major: Chemistry

Under the supervision of Professor Chin Li Cheung

Lincoln, Nebraska

December 2010

Synthesis and Catalytic Activity of Nanostructured Cerium Oxide

Neil Jamieson Lawrence MS

University of Nebraska, 2010

Adviser Chin Li Cheung

Cerium oxide (ceria, $CeO_{2-x}$ where x is 0 to 0.5) has been one of the most widely used heterogeneous catalysts particularly in three way catalytic converters. Most of the catalytic traits can be attributed to two properties of ceria: first, the high mobility and storage capacity of oxygen within the lattice; second, the ease with which cerium changes between $Ce^{3+}$ and $Ce^{4+}$ states. These properties, combined with the abundance of cerium on earth, make ceria a low-cost highly effective alternative to noble metal catalysts. Recent research has been focused on the nanoscale properties of ceria.

The effect on the catalytic activity of cerium oxide caused by varying the density of oxygen vacancy defects (OVD) has not been previously studied experimentally. This is due to the perceived inability to engineer stable defects not attributed to the presence of dopant atoms. It was found that the number of stable OVDs on cerium oxide nanoparticles and nanorods can be increased with annealing at elevated temperatures under low pressure. The oxidative catalytic activity of these nanostructured catalysts was evaluated. Samples with higher densities of OVD were found to have much lower light-off temperatures when compared to that of their bulk counterpart. The chemical equilibrium reactions on the catalysts surface under low pressure were hypothesized to explain the unusual increase in the OVD density of the reported cerium oxide nanostructured catalysts.

Cerium oxide is well known to exfoliate from the surface of cerium metal in the same way that rust exfoliates from iron or steel. A two-step process to fabricate nanoporous ceria membranes via anodization and subsequent calcinations is reported. These membranes have the potential to be used in solid oxide fuel cells and solid-state oxygen sensors. Cerium metal foil was first anodized into adherent porous cerium hydroxide film, followed by calcination for conversion into ceria membranes. These membranes are composed of ribbon-like structures that form the backbone of the porous framework. A proposed anodization model for the growth of the nanoribbons is discussed.

# Table of Contents

# List of Figures

# Acknowledgements

First, I would like to acknowledge my adviser Dr. "Barry" Chin Li Cheung. His support, guidance, and caring have allowed me to begin my journey of learning how to think about and solve problems as a true scientist. He has been an inspiration to me and to my lab mates. I would also like to thank my lab mates especially Joseph Brewer, for their help and support. The discussion provided, and the camaraderie have made my time in and out of the lab wonderful. David Diercks and Nancy Bunce of University of North Texas provided me with wonderful spectroscopy, electron microscopy, and discussion. You Zhou, Han Chen, and Terri Fangman of the University of Nebraska Lincoln Morrison Microscopy Core Research Facility, were always helpful and willing to discuss the results of many experiments. I gratefully acknowledge the Nebraska Research Initiative for funding for these projects. Finally, I want to thank Michelle Lawrence, Jessykah Barron, Jared Hansen and Chad Jones for their help in proof reading my thesis.

## Dedication

Dedicated to my family. Michelle, my loving wife without whom I could not have continued my education, Vivianna and Reed my children who tolerated my frequent absences from home, and my parents Steve and Geri who instilled in me a desire to seek out answers to questions.

# Chapter 1 – Introduction

Today, the world faces a variety of challenges in reducing dependence on petroleum reserves, reducing harmful by-products in manufacturing and transportation, remediating environmental issues, preventing future pollution, and creating safe pharmaceuticals.[7] Catalysts are needed to meet these challenges, but their complexity and diversity demand a revolution in the way catalysts are designed and used.[8] There is a need to move beyond simple improvements to existing catalytic materials and begin to understand the underlying principles so that it becomes possible to predict and then create catalysts for a given set of reactants and products. New opportunities in catalyst design and development are being made possible by breakthroughs in atomic scale measurement, atomic resolution microscopy, and computational modeling. By utilizing these breakthroughs, the challenges of today will be met and those yet to come will be resolved.

## 1.1 Cerium and Cerium Oxide

Included in the rare earths are the fourteen lanthanides along with scandium and yttrium. Of the rare earths, cerium is arguably the most exciting for researchers in the field of catalysis. Cerium is far more abundant in the upper crust, 64 ppm, than any other rare earth elements it is more abundant than copper, 60 ppm, or tin, 2.3 ppm.[9] Its high abundance, combined with excellent catalytic activity for a variety of reactions, makes cerium the element of choice for the automotive industry enabling the catalytic conversion of the exhaust system of automobiles.

The electron configuration of cerium is [Xe] $4f^2 6s^2$ with two common valence state cerium (III) and cerium (IV). Cerium has 30 isotopes whose half-lives are known, with mass numbers 123 to 152. Three stable isotopes: $^{136}Ce$, $^{138}Ce$ and $^{140}Ce$. The most abundant isotope is $^{140}Ce$ at 88.5%. Cerium has a very large liquid range with a melting point of 795 °C to the boiling point of 3443 °C under 1 atmosphere argon.

Cerium metal is tin-like in appearance, soft and ductile. The metal oxidizes easily and rapidly in air with tarnishing being apparent within an hour and the formation of yellow cerium oxide, which easily flakes off of the surface, within 36 hours of exposure to air.

### 1.1.2 Production and Application of Cerium Metal

Rare earth minerals occur in a variety of geological environments. Concentrations exist in igneous and sedimentary rocks. Over 160 minerals are rare earth bearing, but only a few are recovered for commercial production.[15] Bastnasite, carbonatite, loparite, monazite, xenotime and rare earth bearing clays are the major ores mined today. The most important deposits occur in California, Wyoming and Nebraska, United States; Australia, Mongolia and China. Once mined, the ore is subjected to flotation. The rare earth fraction is attracted to surfactants and floats on the surface where it is collected to produce a concentrate.[15] The concentrate is then subjected to a lengthy process involving batch roasting followed by reactions to form an oxide precipitate. Treatments such as liquid-liquid solvent extractions, selective precipitation, ion exchange, and electroplating are used to produce rare earth metals in purity greater than 99.999%.[12, 15] Once refined, cerium metal must be stored in an inert environment to prevent rapid oxidation.

Cerium metal is most commonly used in the ferrocerium firesteel metal alloy used in lighter flints. Metallic cerium is also added in micro-quantities to various alloys as an oxygen and sulfur scavenger. The addition of cerium metal to these alloys can confer a longer operating life by significantly improving their oxidative resistance.

### 1.1.3 Production of Cerium Oxide

Cerium oxide ($CeO_{2-x}$ : x = 0 to 0.5), also known as ceria, is produced by various methods chosen by the desired properties of the product. For bulk materials, to be used without purification, the oxide is collected during the refining process after adding the oxalate to nitric acid. For other materials, a range of precursors are used with a variety of synthetic methods. Common precursors are cerium sulfate ($Ce_2(SO_4)_3$), cerium nitrate ($Ce(NO_3)_3$) ammonium cerium nitrate ($NH_4Ce(NO_3)_4$) and cerium chloride ($CeCl_3$). Cerium hydroxide is a common intermediate of many solvothermal and hydrothermal synthetic processes of cerium oxide.[16] Synthetic methods currently in use are: precipitation, milling, hydrothermal synthesis, sol-gel, surfactant assisted, and spray pyrolysis.[2, 4-5, 10, 14, 17-20]

### 1.1.4 Applications of Cerium Oxide in the Glass Industry

Cerium oxide is used significantly by the glass industry as an efficient polishing agent for most glass compositions and also to prevent the decolorization of glass. These applications consume a significant portion of the cerium oxide products produced annually. The addition of cerium (IV) oxide to the glass melt helps to convert iron to the low visible absorption ion iron (II). The photo stability of pigments is also enhanced by the addition of cerium as it provides the pigments with color fastness and prevents clear

polymers from darkening in the sun. Cerium oxide enhances stability because it has low absorption in the visible light but is nearly opaque in the UV range. This protects the pigments used in glass coloration as most of the damage induced is due to UV light exposure.[14]

### 1.1.5 Applications of Cerium Oxide as a Catalyst

As much as forty percent by weight of the catalyst used for cracking crude oil in refinery operations is cerium and other rare earths. Cerium also has minor uses in other commercial catalysis, such as the production of styrene from ethyl benzene, catalyzed by mixed iron and cerium oxide.[21] Self-cleaning ovens utilize cerium oxide for its self-cleaning properties. The ceria is embedded in the walls and bottom of the oven and acts as an oxidative catalyst when the oven is heated. Cerium oxide is being increasingly used to clean vehicle exhaust streams through direct addition to diesel fuels to reduce sulfur emissions.[14]

### 1.1.6 Applications of Cerium Oxide in the Textile Industry

Cerium compounds can be grafted onto cellulose, wool, starch, and cotton to initiate polarization of vinyl on their surfaces. This improves the mechanical strength, adds resistance to moisture and microorganism attack. These materials are then used in the manufacture of rain gear and similar products.[9, 12, 14]

### 1.2 Catalysis

### 1.2.1 Importance of Catalysis

In the century since Fritz Haber discovered that the introduction of an iron catalyst would accelerate the production of ammonia from nitrogen and hydrogen gases,

research in the area of heterogeneous catalysts has been very active. It is estimated that more than 90% of industrial manufacturing processes worldwide utilize catalysis in one form or another. According to the Food and Agriculture Organization of the United Nations the worldwide demand for nitrogen-based fertilizer will be 154,199 thousand tons in 2011 an increase of 7.3 million tons annually. Virtually all nitrogen fertilizer is produced as ammonia utilizing the Haber-Bosch process, leading to this process being named the "invention of the century."[22]

Catalysis provides a means of changing the rates and of controlling the yields of chemical reactions to increase the amounts of desirable products from these reactions and reduce the amounts of undesirable ones. The reduced emissions of automobiles, and the abundance of fresh food, are made possible by chemical reactions controlled by catalysts. Catalysis is also essential to a healthy economy; the petroleum, chemical, and pharmaceutical industries, contributors of $500 billion to the gross national product of the United States, rely on catalysts to produce everything from fuels and "wonder drugs" to paints and cosmetics.[6, 8]

**1.2.2 Definitions**

Students of chemistry often feel so ingrained that there seems little need to define the terms of the concepts behind catalysis. To avoid any misunderstanding, catalysis will be defined as an increase in the rate at which equilibrium is achieved through the addition of a substance that, once the reaction is at equilibrium, is indistinguishable from its original form. Heterogeneous catalysis involves at least one of the reactants being in a distinct phase from the catalyst. This thesis focuses on reactions in which the catalyst is in the solid phase and the reactants are fluid, either gas or liquid.

### 1.2.3 Heterogeneous Catalytic Mechanisms

### 1.2.3.1 General Heterogeneous Catalytic Mechanisms

Typically, when catalysis occurs on a solid surface and the reactants are fluid, the reaction can be broken into several basic steps: diffusion of the reactants to the catalytic surface, adsorption, diffusion along the surface, formation and breaking of bonds, and desorption.[23-28]

In a metal substrate catalyzed CO oxidation situation (Figure 1), when both carbon monoxide and oxygen are adsorbed onto the surface of the catalyst (a) and (b). The molecules diffuse across the surface (c) until a properly oriented collision, facilitated by the catalyst, occurs. The bond between the oxygen atoms is weakened and a reaction between the oxygen and carbon monoxide occurs (d) and the carbon dioxide diffuses away. The remaining oxygen atom remains adsorbed on the surface of the metal until a properly oriented carbon monoxide molecule adsorbs on the surface of the metal, diffuses to the location of the oxygen, reacts (e), and then diffuses away from the surface (f).[29-30]

### 1.2.3.2 Catalytic Mechanisms of Ceria

The mechanism of catalytic activity on ceria is a subject of much debate. The cited reasons tend to revolve the oxygen storage capacity (OSC) which is largely due to the multivalent nature of cerium and the high mobility of the oxygen vacancies at the surface of the materials. The change in energy for any heterogeneous catalyst is largely a surface effect. The shift between the $Ce^{3+}$ to $Ce^{4+}$ states leads to a high oxygen mobility in ceria lattice, which in turn can lead to a strong catalytic potential.[31-32] Recently the controlled synthesis of functional nano-sized ceria has become almost commonplace.
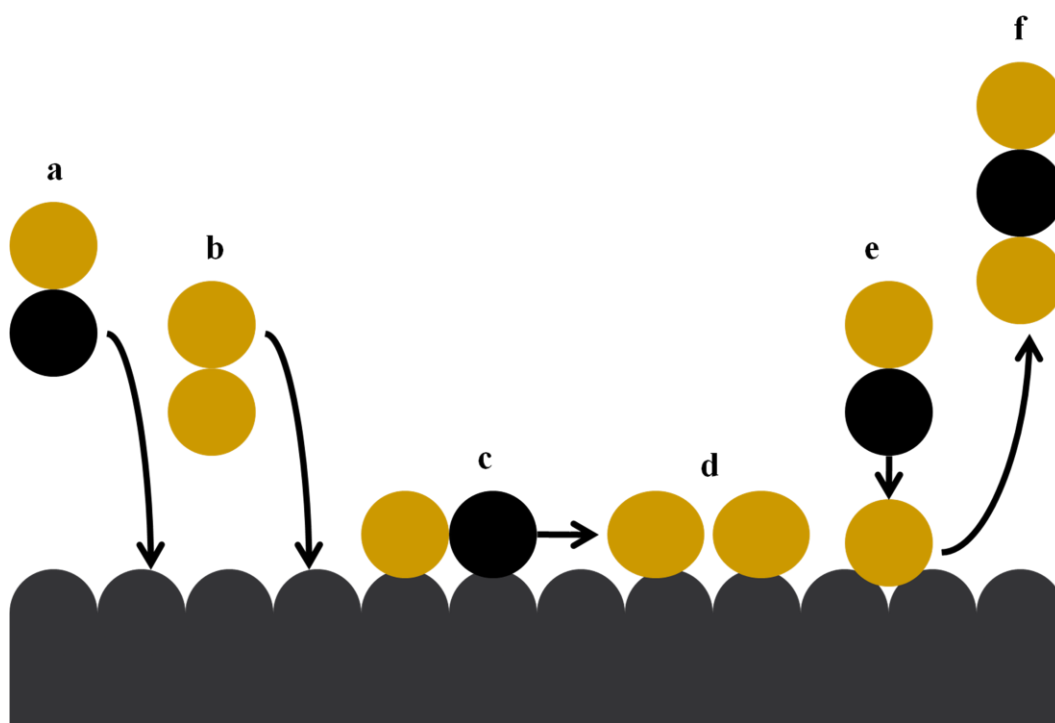
Figure 1 Schematic of CO oxidation mechanism on a metal catalyst

However, many of these materials show very distinct catalytic activity, even from other materials which have similar structures; this is attributed to the effect of defect sites and which crystal facet is exposed.[31, 33-37] These phenomena can be explained by the synthetic method and conditions and by post processing methods used to deliberately introduce defects into the crystal structure (Figure 2). Literature often attributes the catalytic activity of cerium oxide to its high oxygen storage capacity (OSC) which is largely due to the multi-valence nature of cerium. The shift between the cerium(III) ($Ce^{3+}$) to cerium(IV) ($Ce^{4+}$) states leads to a high oxygen mobility in the ceria lattice that in turn leads to a strong catalytic potential.[14, 38-41] Research is focused on the intentional introduction of defects into the lattice through controlling the preferred crystal orientation through controlling synthetic and postproduction parameters. There are many types of lattice defects, all of which can affect the reactivity of the surface of the crystal greatly. These defects, shown in (Figure 2), include vacancies such as OVD (a), self-interstitials (b), interstitial impurity atoms (c) and (d), and edge dislocations (e) and (f).[42]

The degree of oxygen mobility in the ceria lattice can be attributed to the size, dispersion, and quantity of oxygen vacancy defects (OVD).[43-46] The localization of electrons in the empty $4f$ states of the cerium surrounding a vacancy in the ceria support lattice has been demonstrated to form defect sites.[3, 26, 28, 47-48] These only occur around cerium (III) ions and are interpreted to be mobile, as would be expected with the high oxygen mobility. Once subsurface vacancies are introduced into the lattice, the mobility of the vacancies, and thus the defects, is greatly decreased. Vacancy clusters tend to form in the three or six surrounding cerium ions of the materials' surface.
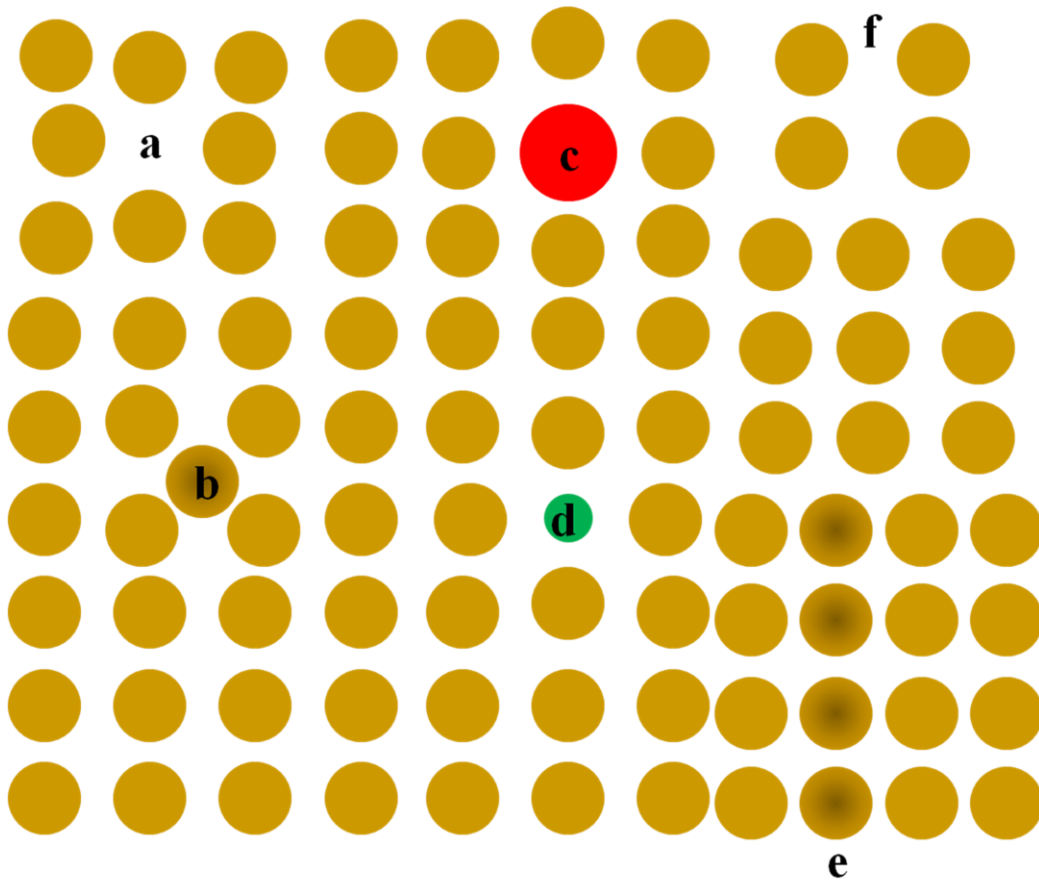
Figure 2 Types of lattice defects

The formation of an oxygen vacancy defect under low partial pressure of oxygen follows the basic steps of the diffusion of oxygen through the lattice. Once the oxygen encounters another favorable oxygen, a bond is formed and the oxygen molecule is able to diffuse away from the surface of the crystal. Each $O_2$ molecule that forms and diffuses away from the surface leaves behind two electrons to be shared between three cerium atoms. This leads to the partial reduction of those cerium atoms to a valency between the 3+ and 4+ states. This usually happens in such a way as to leave behind triads of vacancies with the surrounding nine cerium atoms sharing eight electrons. (Figure 3) The effect of lattice strain has been shown by several groups to increase the activity of metal and metal oxide surfaces.[30, 49-51] One of the most significant proposed reasons for the change in activity of a surface with lattice strain is due to the change in the adsorption energy with respect to carbon monoxide and oxygen. It is notable that the same studies show little increase in the adsorption energy with respect to carbon dioxide.[28, 52] The increase in adsorption energy with respect to oxygen is about five times greater than the increase for carbon monoxide. Additionally, the activation barriers for the dissociation of oxygen and for the formation of carbon dioxide are greatly lowered.

The oxidation of carbon monoxide on a ceria surface is similar to standard heterogeneous catalysis on metal. However, the ease of formation of the oxygen vacancies facilitates the reaction, making this reaction different. (Figure 4) A carbon monoxide molecule adsorbs on the surface of the ceria (a) and readily reacts with surface oxygen then diffuses away as carbon dioxide leaving an oxygen vacancy (b). The presence of an oxygen vacancy (c) allows an adsorbed oxygen molecule to react with the

surface resulting in a weakened bond between the oxygen atoms. A carbon monoxide diffuses across the surface of the catalyst (d) until it encounters the excess oxygen (e) and diffuses away from the surface.[21, 45, 53-56]
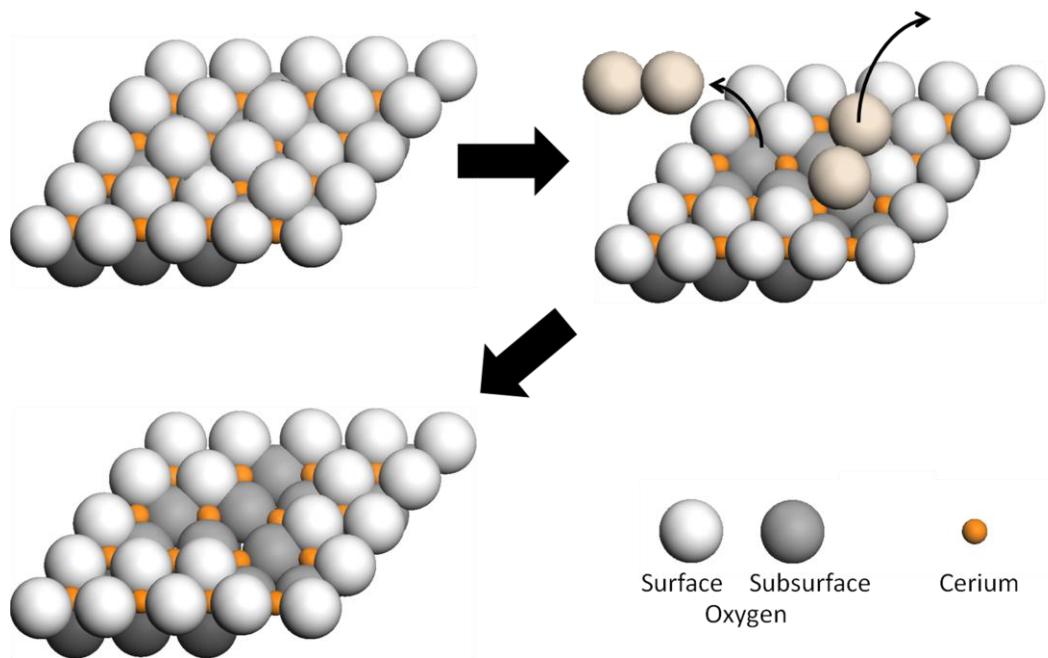
Figure 3 Formation of an oxygen vacancy defect (OVD) in ceria
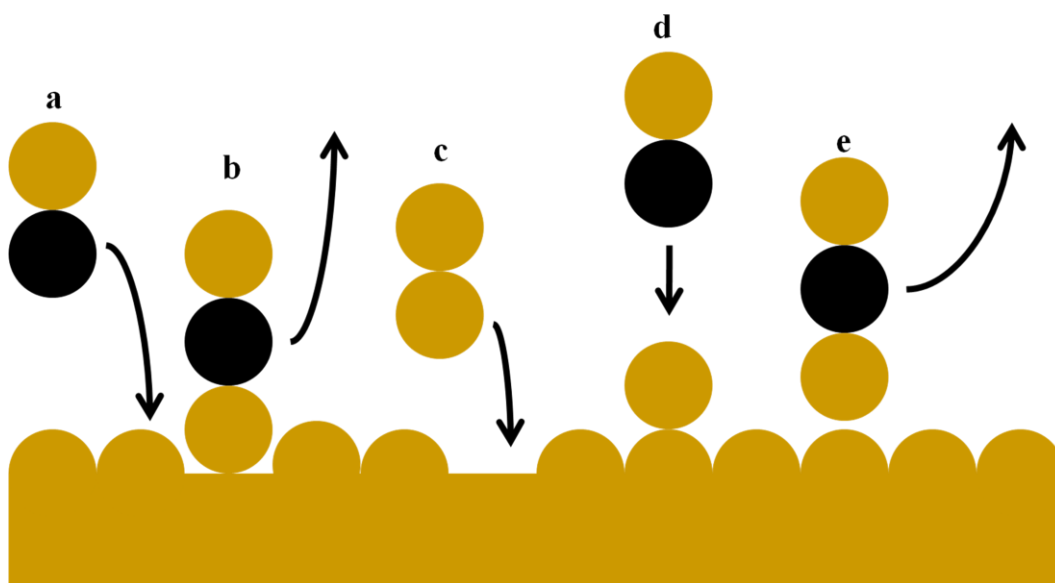
Figure 4 Schematic of CO oxidation mechanism on cerium oxide

**1.3 Bulk Materials Compared to Nano Materials**

In 1959 Richard Feynman gave a groundbreaking talk in which he described what was to become the nano-revolution.[57] In this talk, he stated that it would soon be possible to "arrange atoms the way we want". At the time, few could imagine that this was much more than a thought experiment or a doorway to mere curiosity. In the 40 intervening years, materials designed on the nanoscale have gone from theoretical, to revolutionary, to commonplace in our daily lives. Indeed nanomaterials differ so greatly from their bulk counterparts of identical chemical composition that they have become a field of study on their own.[58]

**1.3.1 Size Effects on Structure and Morphology**

For a 1 $cm^3$ cube of gold, the number of atoms on the surface can be calculated and is very low compared to the total number of atoms in the bulk of the material. When the cube is divided into ever-smaller cubes until there are $10^{21}$ cubes of 1 $nm^3$ all of the gold atoms are on the surface of the cube. Surface atoms possess fewer nearest neighbors and therefore have unsatisfied bonds exposed on the surface. Due to these unsatisfied bonds, they are under an inwardly directed force that leads to the shortening of bond distances between the surface atoms and the bulk atoms. This bond shortening becomes more significant as the ratio of surface atoms to interior atoms increases. This extra energy possessed by the surface atoms leads to changed properties of the materials including morphology, band gap, reactivity, and catalytic potential.

**1.3.3 Reactivity of Nanoparticles**

The reactivity of nanoparticles is closely related to the radius of the curvature of the surface. Imagine taking an atom from the surface of an infinitely flat solid and transfer it to a spherical solid particle of radius $R$. This transfer results in a change in the volume of the particle ($dV$). The change in volume of the particle is equal to the atomic volume ($\Omega$) times the number of atoms transferred ($dn$):

$$dV = 4\pi R^2 dR = \Omega dn \tag{1.1}$$

The work per atom transferred ($\Delta\mu$) is equal to the change in chemical potential ($\mu_c - \mu_\infty$) also equal to the surface energy ($\gamma$) times the change in surface area ($dA$) per the change in the number of atoms transferred:

$$\Delta\mu = \mu_c - \mu_\infty = \gamma \frac{dA}{dn} = \gamma 8\pi R dR \frac{\Omega}{dV} \tag{1.2}$$

Combining this with equation (1.1) gives us:

$$\Delta\mu = 2\gamma \frac{\Omega}{R} \tag{1.3}$$

which is known as the Young-Laplace equation that describes the chemical potential of an atom in a spherical surface with respect to a flat reference surface. As the radius of the particle decrease the chemical potential increases. This leads to a more reactive surface. This is one of the most significant ways in which nanomaterials differ from bulk materials.

## 1.4 Defect Engineering in Catalysts

Engineering of catalysts is typically focused on the shape, size, and components of the catalysts. Though it is commonly accepted that defects are very important to the activity of a catalyst, little experimental data has been presented about the use of

engineering oxygen vacancies to enhance the catalytic activity of the ceria.[31, 33-34, 36-37, 59-62] This lack of discussion has been primarily due to the inability to engineer in or qualitatively and quantitatively define the OVD sites. Much effort has been spent on engineering the size, structure, and exposed facets for ceria based catalysts.

Cerium oxide ($CeO_2$ and $Ce_2O_3$) has been shown to be a very important material in three-way catalysis as well as in the catalysis of other reactions; additionally the relative abundance of cerium makes it an economically exciting alternative to noble metal catalysts. In the oxidative catalysis of carbon monoxide the presence of OVDs and other lattice defects play a very important role in the reactivity of the surface. Scanning tunneling microscopy (STM) studies have shown both surface and subsurface OVD sites play an important role in the enhancement of the oxidation of CO by ceria. Additionally $Ce^{3+}$ atoms located near the OVD sites appear to actively participate in the reaction by lowering the binding energy of the products and reactants.

Nanoscale catalysts which have been engineered with one or more dimensions in the nanometer size range are an emerging area of study for the advancement of catalyst design. While other groups have engineered ceria down to the nanoscale with great success, little research has been published on engineering defects into nanoscale ceria. For example, dendritic, engineered multi-faceted, and well defined structured ceria have all been shown to drastically affect the oxidative catalytic activity compared to bulk ceria. The enhanced catalytic activity of these nanoscaled materials is often attributed to the specific facets that are exposed. Other reported advantages of nanoscale materials are: increased surface area, and enhanced surface to volume ratios. While much effort has been aimed at creating selected facets and shapes, little effort has been spent on creating,

quantifying, and determining the effect of engineered OVDs and other defects at the nanoscale.

## 1.5 Thesis Overview

In this thesis, two synthetic methods for the preparation of cerium oxide with nanoscale features will be presented. In Chapter 2, a method for the preparation of cerium oxide membranes from cerium foil utilizing anodization will be presented and discussed. In Chapter 3, a method for the preparation of cerium oxide nanorods using hydrothermal synthesis will be presented and discussed. A method of modulating the density and stability of OVD sites on nanoscale cerium oxide will be proposed in the latter part of Chapter 2. The principles associated with the stabilization of these sites will be discussed especially in relation to the catalytic oxidation of carbon monoxide will be presented in Chapter 4. Finally, future work will be proposed in Chapter 5.

## Chapter 2 Nanoporous Ceria Membranes

### 2.1 Introduction

A method of efficiently producing membranes of exfoliating oxides has been sought for many years.[63-64] These membranes can be used in a variety of catalytic applications. The most interesting, given current energy concerns, is as the catalytic membrane in fuel cells.

### 2.1.1 Solid Oxide Fuel Cells

Solid oxide fuel cells (SOFC) (Figure 5) are being actively studied due to their promising future in large-scale high power applications including: centralized electricity generation, and automotive power plants as an alternative method for extracting the energy from stored hydrogen.[64-65] SOFC are particularly appealing when produced to generate between 2kW and 20 MW. An operating temperature of 1000 °C can be utilized with a catalyst to convert natural gas into a very clean fuel stream for the SOFCs. Ideally, an SOFC membrane will have several characteristics: efficiently catalyze the reaction of interest, they should be hydrophobic to rapidly shed the water produced and return to a state of readiness, a very large surface area, and should be resistant to fouling when introduced to an impure fuel stream. SOFC membranes made from cerium oxide are of interest due to their ability to act as a three-way catalyst. The primary function of converting hydrogen and oxygen to water and electricity can be accomplished readily. If the fuel stream contains hydrocarbons which need to be oxidized, or excess carbon monoxide which needs to be combusted, these contaminants are also converted without fouling the membrane.

$$H_2 + O^{2-} \longrightarrow H_2O + 2e^-$$

or

$$CH_4 + 4O^{2-} \longrightarrow CO_2 + 2H_2O + 8e^-$$

$$\frac{1}{2}O_2 + 2e^- \longrightarrow O^{2-}$$
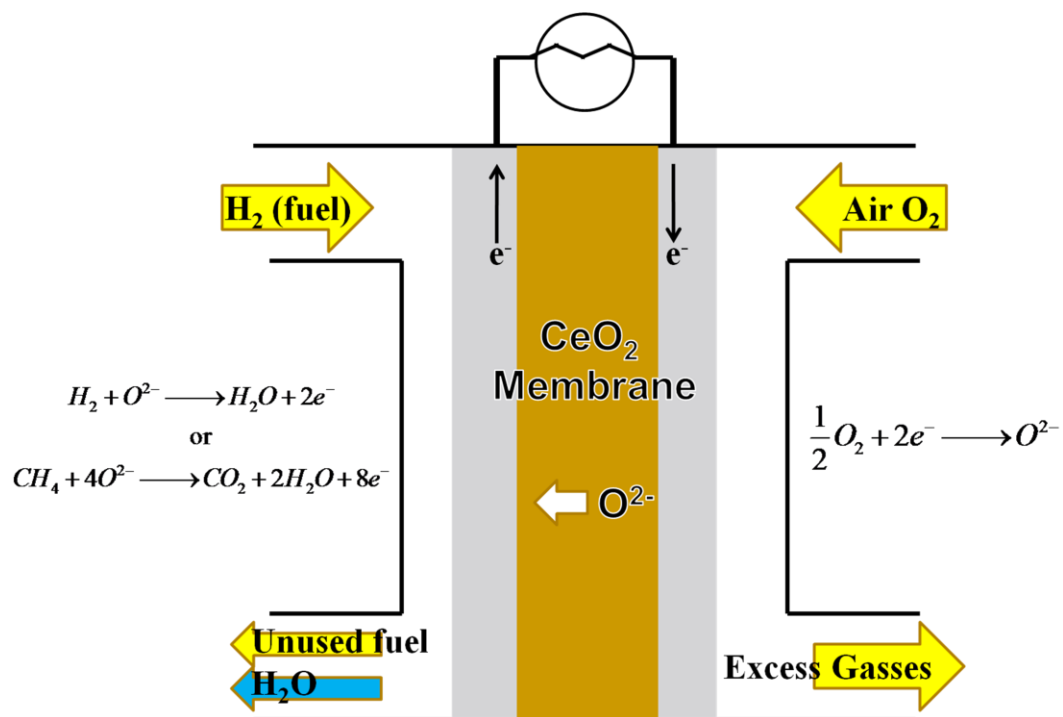
Figure 5 Solid oxide fuel cell schematic

Two major obstacles lie in the path of utilizing cerium oxide as a SOFC membrane. First, it is a high-κ material which is inefficient at transporting electrons away from the reaction site to the conductors. The lack of conductivity can be circumvented by applying a conductive material to the surface of the membrane. Second, $CeO_{2-x}$ is an exfoliating oxide. The need to make a membrane that does not exfoliate will be dealt with in this chapter.

## 2.1.2 Formation of Porous Membranes by Anodization

The creation of a membrane consisting only of ceria has been hampered by the difficulty of anodizing metals with exfoliating oxides. Since the 1920's, anodization has been commonly used to synthesize a wide variety of porous films on metal surfaces.[35] For example, anodization is frequently used to form a protective oxide layer directly on aluminum and titanium surfaces (Figure 6). Anodization of the metal foil has also been used as a method to make metal oxide membranes with nanostructures on the surface of or throughout the materials. The anodization of metals whose oxides exfoliate has been problematic when it comes to generating protective layers. Cerium is such a metal and has not been previously reported to form a useful protective anodized layer or membrane. The two existing models for anodization are the aluminum model in which a metal foil is converted directly to the oxide; and the zinc model in which the foil is converted to either a phosphate or a sulfate.

In this chapter an anodization model, different from either that of aluminum or zinc, is proposed. In this model, the metal cerium is converted to a hydroxide polymer (Figure 7) that incorporates both the ions from the polymer and the reduced metal atoms at the interface. The adhesion of the membrane formed to the metal surface allows for the
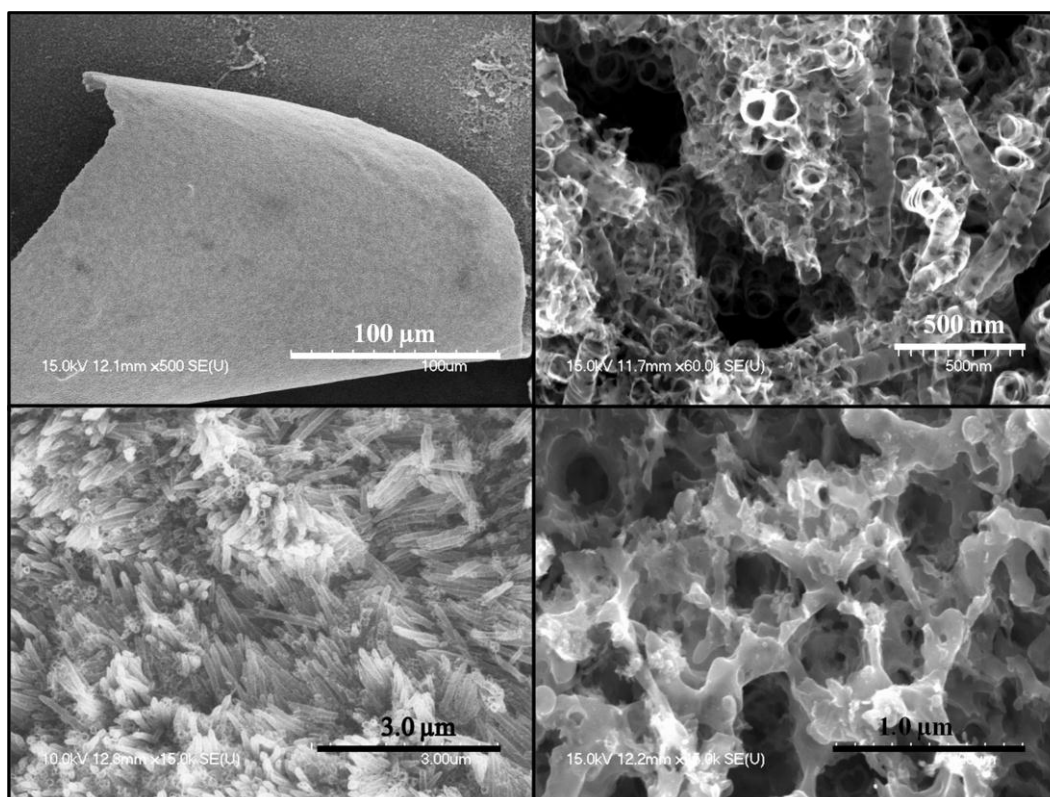
Figure 6 Anodized TiO$_2$
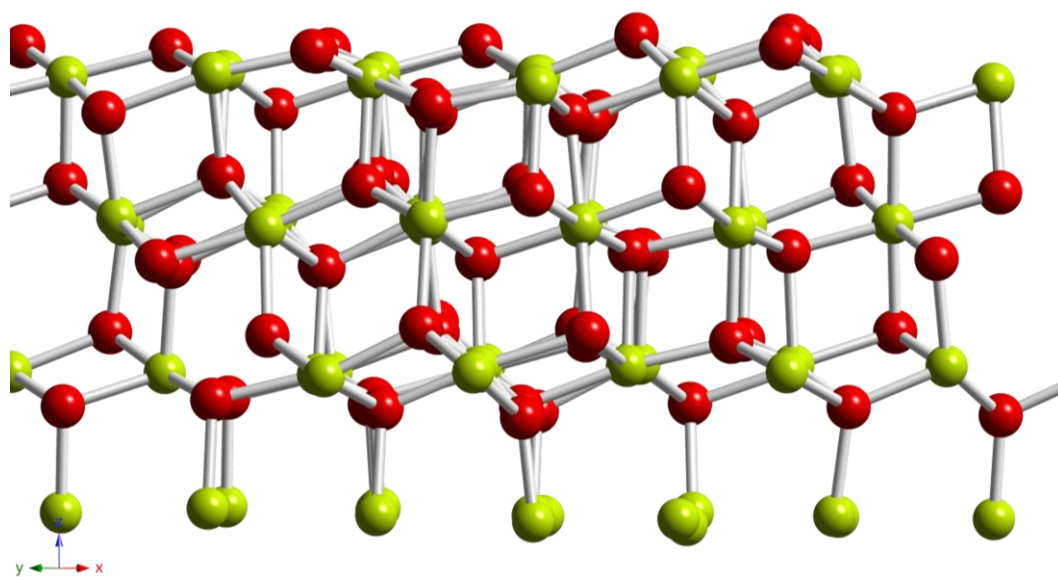
Figure 7 Cerium hydroxide inorganic polymer

buildup of said membrane. This strategy has the potential to lead to huge scientific and commercial progress and applications in the fields of protective coatings and the manufacture of oxide membranes.

## 2.2 Materials and Methods

Cerium metal foil (0.25mm thick, 99.9% Alfa Aesar, Ward Hill, MA) was first cut into 1 cm x 1cm squares and polished with 1 μm diamond grit (BUEHLER, Lake Bluff, IL)until a mirror-like finish was achieved. The samples were sonicated in acetone for 15 min to remove any remaining diamond grit particles and then are dried with nitrogen. The samples were then anodized in a two-electrode cell with the cerium foil as the anode and a 1 cm × 1 cm platinum foil as the cathode. The electrolyte solution was composed of ethylene glycol (99.5% Sigma Aldrich, Milwaukee, WI), ammonium hydroxide (29.56% aqueous solution, Fisher Scientific, Fair Lawn, NJ) and water. All water used in this experiment was Ultrapure water of >18 MΩ resistance and filtered with 0.22 μm membranes. The anodization was accomplished by applying a constant current of 100 μA with a source meter (Keithley 2410, Keithley Instruments Inc. Cleveland, OH) for 160 h. The membrane was considered fully anodized once the applied potential at 100 μA reached the limit of the source meter (1100 V). The membrane was then rinsed thoroughly with ethanol, dried under a nitrogen stream and immersed in a 100 mL ethanol bath for 12 h. The ethanol bath was gently stirred to facilitate the removal of remaining traces of electrolyte from the membrane structures. Afterwards, the sample was dried with a gentle stream of dry nitrogen. Conversion of the samples into cerium (IV) oxide was achieved by calcination at 400 °C for 2 h under a flow of 100 standard cubic centimeters per minute (SCCM) dry air inside a 1" quartz tube furnace under partial

vacuum at an operating pressure of 0.12 Torr. The temperature of the furnace was increased at a rate of 0.5 °C/min to control the calcination rate of the structures and to aid in the gentle evaporation of any remaining solvent.

The optimal conditions under which the anodization of the cerium foil created a self-adherent membrane with ribbon-like structures were constant current of 100 μA, 0.15 M $NH_4OH$ in a mixture of 10 % v/v water in ethylene glycol at room temperature. The anodization process took about 160 h until the cerium foil was fully anodized and clearly showed two distinct membranes had formed back to back of approximately one half of the thickness (100 μm) of the original cerium foil each. While constant potential conditions and higher constant current conditions were attempted, these conditions failed to achieve results of greater than a few tens of nanometers. Once the foil had been anodized and the solvent exchanged with ethanol, the membrane was calcined at 400 °C (ramp rate of 0.5 C/min) for 12 hours under 100 SCCM flowing dry air at 0.1 bar this assisted in the final conversion of the membrane to cerium (IV) oxide as demonstrated by XRD data, shown in Figure 8. Additionally, this allowed the sample time to anneal and become more uniformly crystalline.

In a typical experiment, a cerium metal foil (1 cm$^2$, 0.25mm thick, 99.9% Alfa Aesar, Ward Hill, MA) was anodized at constant current of 100 μA in a two-electrode cell configuration with a platinum cathode to create a porous membrane. The optimal electrolyte solution was composed of 0.15 M ammonium hydroxide ($NH_4OH$) in a mixture of 10 % v/v water in ethylene glycol. The sample was considered to be fully anodized once the potential reached 1000 V. Formation of vapor filled "bubbles" (cavities) was observed on the surface of the foil during the entire anodization process.

Typically, 160 hours were required to fully anodize the foil sample. The as-anodized sample was bathed in stirring 200-proof ethanol overnight to remove the ethylene glycol inside the pores. The sample was then calcined in a 1"-tube furnace at 400 °C in a stream of 100 SCCM dry air at 0.1 Torr for 15 h.

During the process of anodization, the cerium metal is anodized to $Ce^{3+}$ ions and the $Ce^{3+}$ ions react with hydroxide ions in the solution to form a cerium (III) hydroxide ($Ce(OH)_3$) polymer, at the same time $Ce_2O_3$ is also forming on the surface of the foil. The ammonia and water in the electrolyte will also react with the cerium hydroxide and the cerium (III) oxide to form $Ce$-$NH_3$-$H_2O$ complex and the complex will dissolute into the electrolyte and this dissolution process will help the growth of the nanoribbon structure. The formation of the ribbon-like structure is likely due to the formation of the $Ce$-$NH_3$-$H_2O$ complex and the oxygen bubbles at the anode (Figure 13).The formation of $Ce$-$NH_3$-$H_2O$ complex causes the dissolution of the cerium hydroxide-cerium (III) oxide layer. A multi-stage formation mechanism for the porous anodized cerium foil structures with "ribbon-like" backbone framework can be deduced from the experimental observations and possible electrochemical reaction scheme (Scheme 1). In the initial stage of the anodization, cerium metal was electrochemically oxidized to cerium (III) ions ($Ce^{3+}$). At the metal surface, the formation of soluble complexes ($[Ce(NH_3)_{12-x}](OH)_x)^{[14]}$ led to pitting of the metal foil surface. Electric fields enhanced by the high curvatures of the pits possibly caused an increase in the pit size. The $Ce^{3+}$ ions reacted with hydroxide ions to form $Ce(OH)_3$ polymers. The ammonium cations likely complexed with $Ce^{3+}$ ions to form $Ce$-$NH_3$-$H_2O$ soluble chemical species. The formation of this complex possibly caused the dissolution of the cerium (III) hydroxide.
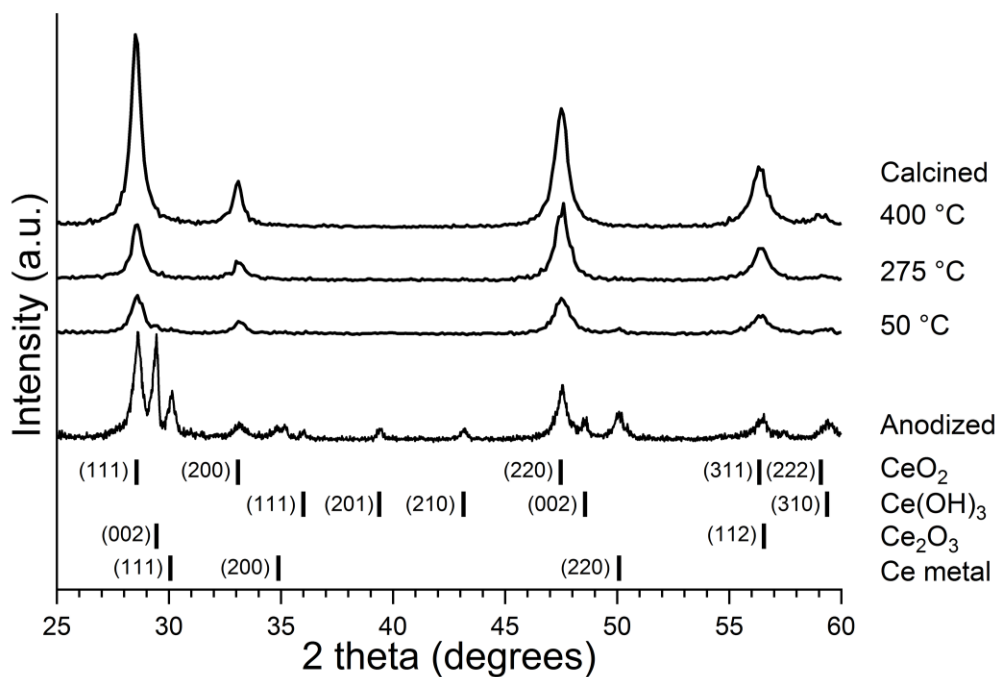
Figure 8 XRD patterns showing the transition of as-anodized cerium foils

From simple hexagonal cerium (III) hydroxide (Ce(OH)$_3$) to fluorite-structured ceria (CeO$_{2-x}$) as the calcination temperature increases 50, 275 to 400 ˚C. (Bottom) Vertical lines showing peak indexes of CeO$_2$, Ce(OH)$_3$, Ce$_2$O$_3$ and α-Ce from the corresponding JCPDS data.

An increase in the ammonia concentration of the electrolyte was found to produce a decrease in the density and thickness of the "ribbon-like" structures. The cerium anode simply appeared to dissolve into the electrolyte solution. This was likely caused by the increased formation rate of the soluble ammonia complexes which competed with the precipitation and formation of the cerium hydroxide framework. However, if the concentration of ammonium ions was very low or the ammonium ions were replaced by sodium ions, the cerium oxide was observed to form, and then exfoliate from the cerium foil. Therefore, the concentration of $NH^{4+}$ ions is critical to the proper formation of the membrane.

At the surface of the cerium foil, oxygen was produced in the oxidation reaction and cavities (vapor filled bubbles) were observed trapped in the porous matrix during the anodization process. The radius ($r$) of a cavity before it left the surface of a solid is a function of the buoyancy of the trapped vapor ($P_{in}$) being resisted by the pressure of the liquid ($P_{out}$) and the surface tension ($\gamma$) causing the adhesion of the cavity to the solid. The use of an electrolyte with a surface tension much less than that of water favored the formation of smaller cavities as indicated by the Young-Laplace relationship.[15]

$$r = \frac{2\gamma}{P_{in} - P_{out}}$$

The formation of the low-solubility $Ce(OH)_3$ precipitated around the cavities, leading to the growth of the thin "ribbon-like" structures of the porous framework. As the cavities of trapped gas increased in size, they eventually escaped, leaving voids adjacent

to bare metal and allowing the continuation of the anodization process. Therefore it was necessary to reduce the surface tension of the electrolyte to reduce the pore size to the desired scale.

Current density appears to affect the growth rate of the "ribbons-like" structures. At a fixed current, the thickness of the cerium hydroxide porous structures increased at a constant rate. An increase or decrease in applied current was found to change the film growth rate of growth proportionally. The pore size was observed to increase with an increase in current density (Data not shown). Similar to the case of anodizing porous silicon, once a threshold current level was reached, the pore diameters of the anodized structures became too large that a smooth surface was obtained instead.[16]

## 2.3 Membrane Characterization: Morphology, Water Contact Angle, and Chemical Composition

### 2.3.1 Surface Morphology

The morphology of the processed samples was investigated by field emission scanning electron microscopy (FE-SEM, Hitachi S4700, Hitachi High Technologies America, Inc., Pleasanton, CA). The crystal structures of the samples were studied by Rigaku D/Max-B diffractometer equipped with Cu Kα X-ray source of average wavelength 1.544 Å (Rigaku America, The Woodlands, TX). Confocal Raman microscopy on the samples was performed with a HR800 confocal Raman microscope (Horiba Scientific, Kyoto Japan, LabRAM) using a 20 mW 632.8 nm He-Ne laser.

### 2.3.2 Water Contact Angle

Contact angle measurements were performed on an AST VCA Optima (AST Products Inc., Billerica, MA) using a 0.25 µL drop size and utilizing the AST software to perform angle measurements. The AST software was used for the contact angle measurements in the recorded optical images. The surface morphology of the anodized $CeO_2$ membrane was studied using field emission scanning electron microscopy (FE-SEM), transmission electron microscopy (TEM) and high-resolution transmission electron microscopy (HRTEM). Figure 9 shows the typical surface and cross-section morphology of the anodized and calcined $CeO_2$ membrane. From the SEM images, ribbon-like structures are demonstrated to have grown on the surface of the membranes. These ribbon-like structures were shown by HRTEM to be slightly polycrystalline with the (111) lattice spacing being the most prominent.

The contact angle is measured to determine the surface structure of the anodized $CeO_2$ membrane. By using Cassie and Baxter's theory, as further studied by Yoshimitsu et al[66-67], the area fraction of the solid-liquid interface could be determined indicating the aspect ratio of the $CeO_2$ membrane structure. The equation describing the contact angle θ' of a rough hydrophobic surface trapping air in the hollows of the rough surface is as follows: (Cassie-Baxter model)

$$\cos\theta' = f\cos\theta + (1-f)\cos 180°$$
(2.1)

where $f$ is the area fraction of the solid-liquid interface and $(1-f)$ is that of the solid-air interface. From the result, (Figure 10) the anodized $CeO_2$ membrane with nanostructure after calcination has a contact angle θ' of 113° and the membrane without nanostructure on it has a contact angle θ' of 39°. By using these data, the area fraction f is 0.62.

The calculation of the surface area fractions from top view SEM images of the porous ceria membranes was accomplished using the NIH software package Image-J.[68] For a typical top view SEM image of a porous ceria membrane (Figure SI-4a), the ridges between the pores are shown as the light shaded areas whereas the pores (cavities) are shown as the dark shaded areas. When a water droplet is dispensed on the porous membrane, the portion of surface area in contact with the water is composed of the ridges and upper portions of the pore structures. The Image-J software allows setting of a relative threshold brightness ratio between the structures with different shades in the SEM images (Figure 11) and converts all the apparent pore area to appear as white and the rest as black. The process was automated using Image-J's built in scripting language as illustrated in Program 1 for our contact surface area estimation (See below). Following the conversion of the image into white areas (non-contact pore) and black areas (possible water contact surface area), Image-J calculates and reports these two apparent surface areas. The mean surface area fraction which describes the fraction of apparent surface area possibly in contact with a water droplet is estimated to be $0.51 \pm 0.03$. Owing to the irregularity of the ceria membrane surface structures, this mean surface area fraction is likely to be underestimated using this apparent surface area estimation method. Nonetheless, visual inspection appears to match this estimated value.
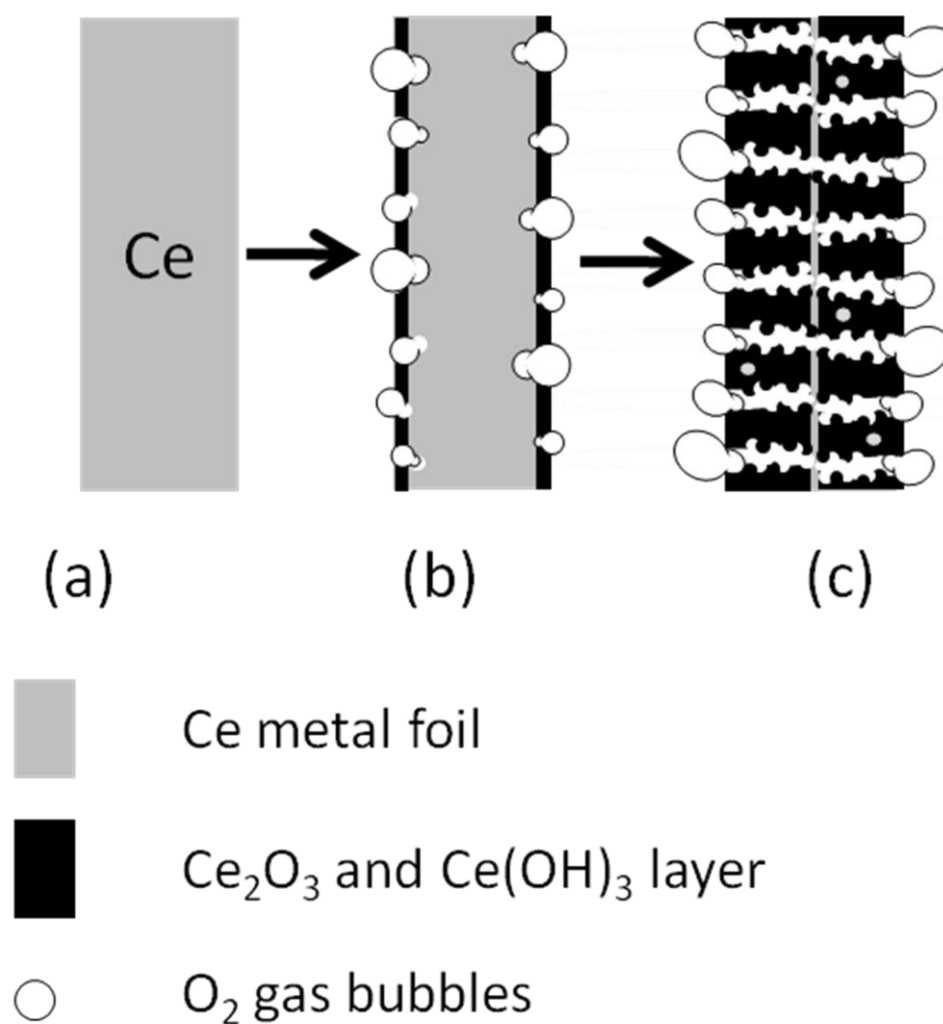
**Schematic 1** Proposed mechanism for the formation of the porous anodized structures from a cerium metal foil. Gray is cerium metal and black is the anodized complex. The cerium metal acts as the anode in the electrochemical cell. As a complex layer begins to form, vapor filled voids (cavities) or "bubbles" form on the surface and create pathways to the metal, allowing the diffusion of reactants to the metal surface. Pores are formed from volume changes due to the formation of the cerium hydroxide. The formation of gas cavities allow the reaction to continue to completion. Small deposits of unoxidized metal may be left as shown in the final stage of the anodization.

The crystal structures of the anodized cerium foil and their transformation by calcination were characterized by x-ray diffraction (XRD) (Figure 2) and indexed against JCPDS data.[*] The XRD pattern of a fully anodized cerium foil suggests that the anodization process transforms the cerium metal foil into *P63/m* hexagonal cerium (III) hydroxide ($Ce(OH)_3$) which oxidizes to *P$\bar{3}$m*1 hexagonal $Ce_2O_3$. The pattern also indicates the presence of a trace amount of $\alpha$-Ce metal which implies that some cerium metal may be preserved between the pores (figure 13-c). Small deposits of metal are likely located in areas where the hydroxide thickness of the pores limits the oxidation at the applied potential. The XRD patterns of anodized samples calcined at 50, 275 and 400 ˚C were also collected to verify the transformation of the anodized samples into cubic *Fm$\bar{3}$m* ceria. Compared to the XRD pattern of the as-anodized sample, the relative intensities of diffraction peaks belonging to the cerium hydroxide and metal in the XRD pattern of the sample calcined at 50 ℃ decreases significantly. For samples calcined at higher temperatures, diffraction peaks of the cubic fluorite structure are dominant in the corresponding XRD patterns. There were no indications of metallic cerium in these patterns. Only the XRD pattern of the sample calcined at 400 ℃ shows no satellite peaks belonging to $Ce(OH)_3$ and hexagonal $Ce_2O_3$, indicating a complete conversion of the sample into fluorite ceria.

Raman scattering spectrum (Figure 12) of the porous $CeO_{2-x}$ membrane displays a peak near 462 cm$^{-1}$, which is typically assigned to the $T_{2g}$ ($F_{2g}$ in some tables[10]) mode of the Ce-O vibrational unit with $O_h$ symmetry.[11] No other significant peaks are found in this spectrum, indicating that the annealed membrane does not have a significant number of lattice related defects.[12]
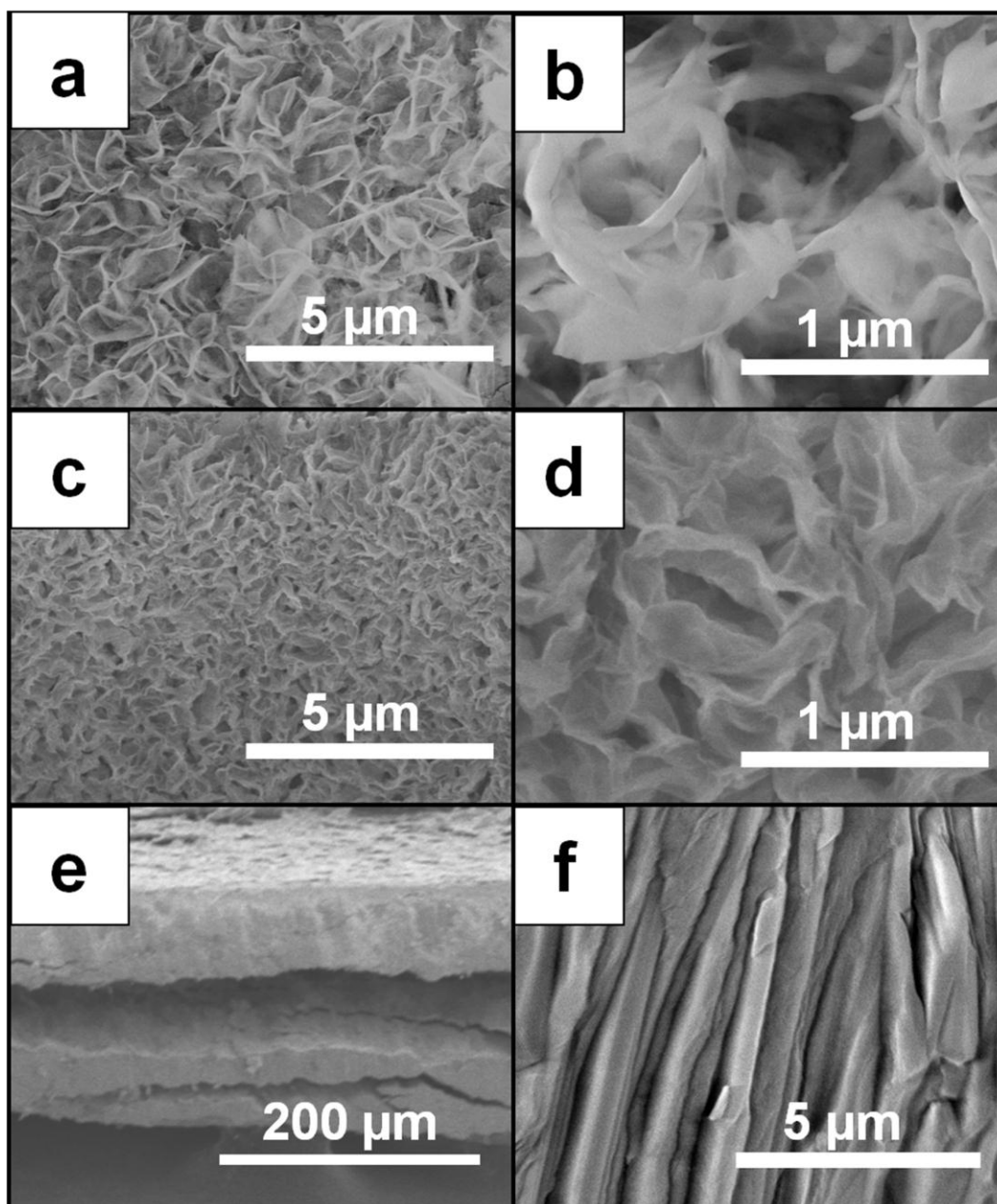
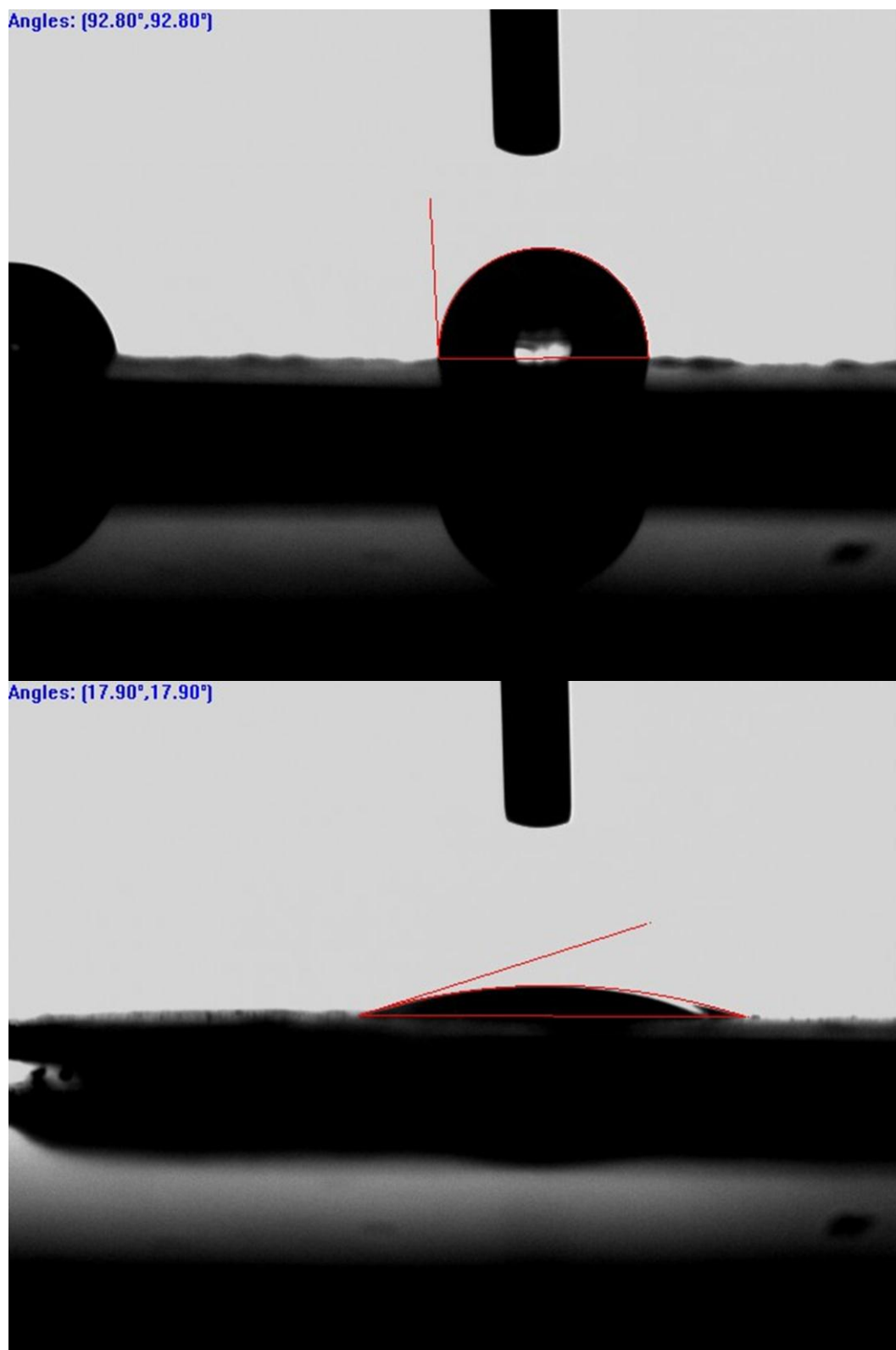Figure 9 Microscopic images of anodized cerium membrane

Figure 10 Water contact angle on anodized cerium membrane
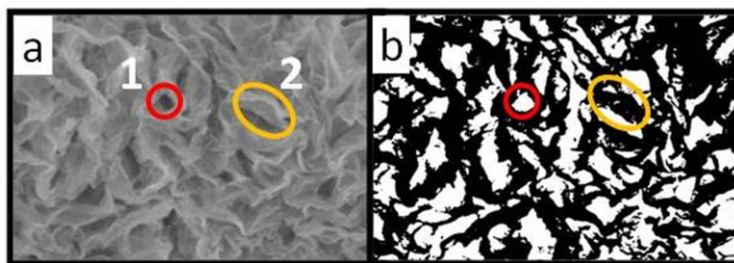
Figure 11 Microscopic images of anodized cerium membrane
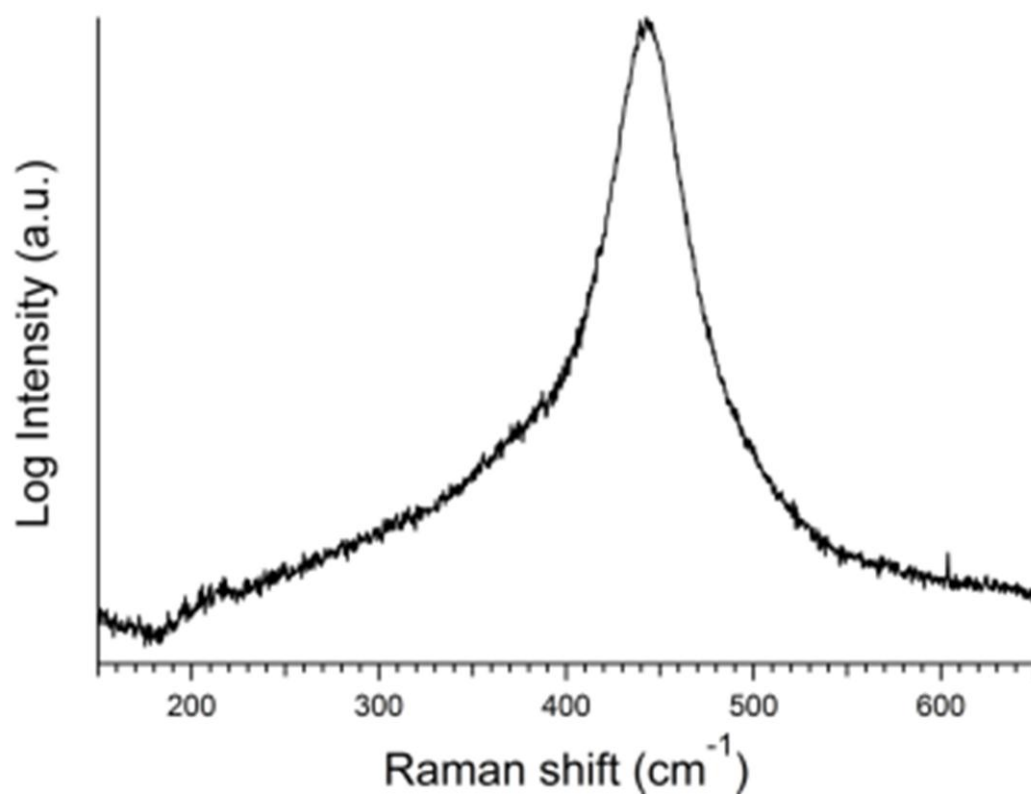
Figure 12 Microscopic images of anodized cerium membrane

converted to $CeO_2$. The calcination process consists of several steps. The components of the anodized membrane before calcination are $Ce(OH)_3$ and $Ce_2O_3$ (according to the $Ce(OH)_3$ (101) (201) peaks and $Ce_2O_3$ (101) (110) peaks). After drying at 50 ℃ for 15h, the intensity of the $Ce(OH)_3$ peaks decrease but the (101) peak of $Ce_2O_3$ remain and the (111) (220) and (311) peaks of $CeO_2$ become the major ones. All of that indicated most of the $Ce(OH)_3$ is converted into $Ce_2O_3$ and $CeO_2$.

## 2.4 Mechanism

According to the experimental results one possible mechanism for the formation of the nanoribbon-like structures (

Figure 13) involves the formation of a complex polymer incorporating the surface atoms of the cerium foil with the hydroxide produced through electrolysis and the ammonium cation. The Ce atom serves as the center atom and $OH^-$, $NH_3$ ($NH^{4+}$) and $H_2O$ serve as the ligands to form a $CeX_6$ complex ($[Ce(NH_3)_{6-x}](OH)_x$). These complexes dissolve into the electrolyte digging holes or grooves on the $Ce_2O_3$ and $Ce(OH)_3$ surface making the nanoribbon structure grow. As this polymer forms it branches as the ammonium ligands are replaced by water ligands. The formation of gas bubbles on the reaction surface increases the size of the pores between the sheets where the polymer branches. The oxygen gas bubbles formed at the anode do not only react with the Ce metal foil to form the $Ce_2O_3$, but also serve as the template during the anodization process. The size of these bubbles was expected to influence the pore size.

During anodization, the voltage increased due to 3 factors: the increasing thickness of the oxide layer, the decrease in the amount of electrolyte in solution and the
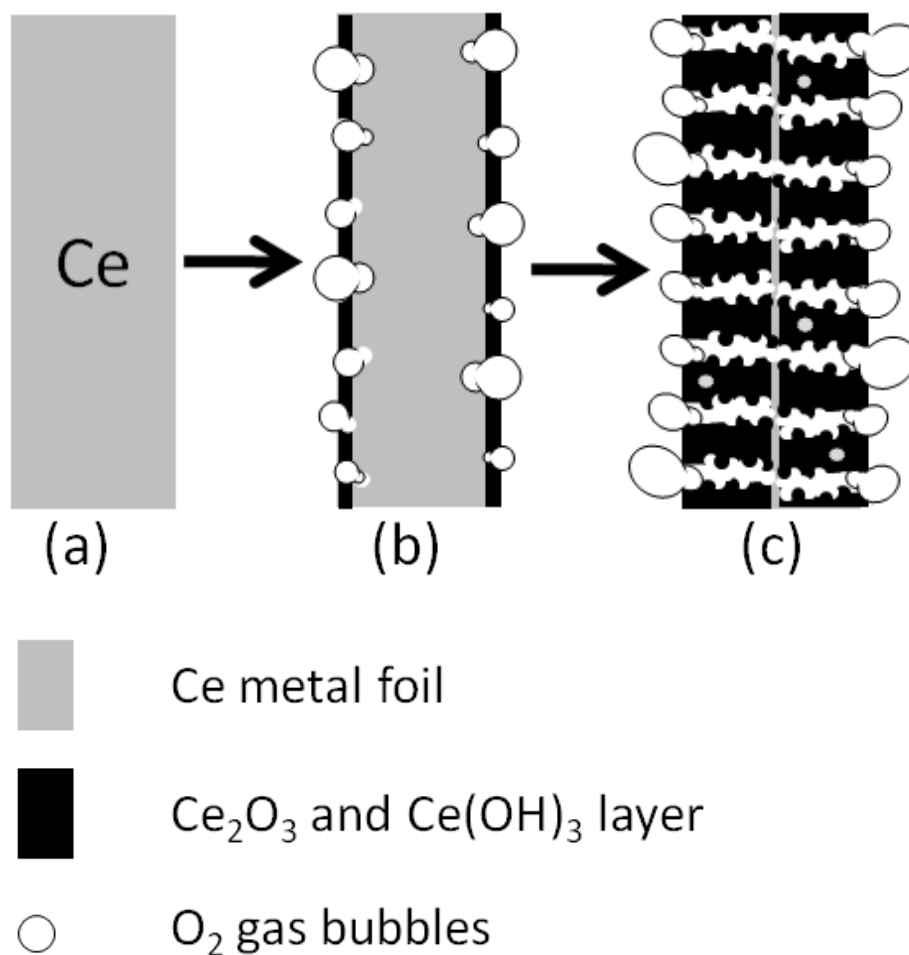
Figure 13 Proposed mechanism for the formation of the porous anodized structures from a cerium metal foil.

Gray is cerium metal and black is the anodized complex. The cerium metal acts as the anode in the electrochemical cell. As a complex layer begins to form, vapor filled voids (cavities) or "bubbles" form on the surface and create pathways to the metal, allowing the diffusion of reactants to the metal surface. Pores are formed from volume changes due to the formation of the cerium hydroxide. The formation of gas cavities allow the reaction to continue to completion. Small deposits of unoxidized metal may be left as shown in the final stage of the anodization

increase in the number and size of $O_2$ bubbles forming on the surface of the cerium, all of which increase the resistance.

Table 1 lists our proposed series of reactions for the formation of the polymeric substrate. As we can see reactions (5) and (6) predict that an increase in the ammonium concentration will increase the rate of dissolution of $Ce(OH)_3$ and $Ce_2O_3$, also higher ammonium concentration will provide lower resistance causing a lower anodization potential. If the rate of dissolution is greater than the rate of the formation of the nanoribbon structures then the structures will not form. On the other hand, if the concentration is too low the formation of the $[Ce(NH_3)_{10-x}]^{3+}$ complex is present, leading to the formation of $CeO_{2-x}$, which simply exfoliates from the surface. The morphology of the anodized cerium oxide membrane is determined by a variety of factors; however, the thickness of the membrane thickness is solely a function of time. FESEM showed that typically an as-fabricated anodized ceria membrane surface is composed of ribbon-like structure. The average ribbon thickness is 20 to 30 nm and the size of the pores between the ribbons is about 150 nm. However, the ribbons' thickness of the calcined samples increases to ca. 50 nm while the average pore size of the film remained almost the same (160-170 nm). The slow temperature ramping rate in the calcination process apparently promotes the growth of the ribbon structures after calcination. Cross-sectional FESEM images of completely anodized membranes illustrates that the thickness of the membrane is ca. 100 μm.

Current density determines the growth rate of the structure; with increased current, the growth rate of the nanoribbons is increased leading to larger pore diameters of the structure. A higher anodization current causes the aspect ratio of the ribbon

$$Ce \rightarrow Ce^{3+} + 3e^-$$

(1)

$$Ce^{3+} + 3OH^- \rightarrow Ce(OH)_3$$

(2)

$$O_2 + 2H_2O + 4e^- \rightarrow 4OH^-$$

(3)

$$4Ce + 3O_2 \rightarrow 2Ce_2O_3$$

(4)

$$Ce(OH)_3 + xNH_3 \rightarrow [Ce(NH_3)_x]^{3+} + 3OH^-$$

(5)

$$Ce_2O_3 + 2xNH_3 + 3H_2O \rightarrow 2[Ce(NH_3)_x]^{3+} + 6OH^-$$

(6)
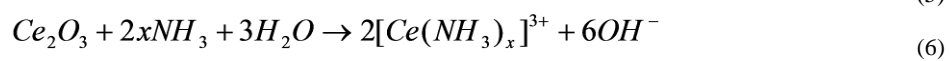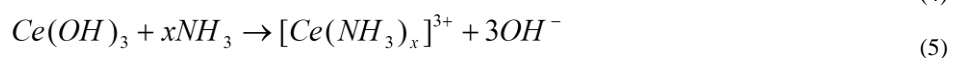
Table 1 Proposed series of reactions for the formation of the polymeric substrate

structure to be decreased. Other factors which affect the growth of nanoribbon structure

are: the distance between the electrodes, electrode shape, and active vs. passive mixing of

the electrolyte solution however the major factors are the ones discussed above.

### 2.4.1 Image-J program for determining surface area

Program 1 – Calculate the area on nanoribbons

```
// "Calculate the area on Nanoribbons"
//
// This script will batch process the .tif images in a given folder and subfolders
// and will calculate the ratio of the area of the ribbon edges to the area of the pore.
// This is accomplished by converting the image to binary (black and white) and reporting
// the percentage of the area that is above the threshold for conversion to black.
// the threshold level can be set manually if the contrast of the original image is too low.
//
// This macro batch processes all the files in a folder and any
// subfolders in that folder.

  requires("1.33s");
  dir = getDirectory("Choose a Directory ");
  sav = getDirectory("Choose a Save Directory ");
  setBatchMode(true);
  count = 0;
  countFiles(dir);
  n = 0;
  processFiles(dir);
  print(count+" files processed");

  function countFiles(dir) {
   list = getFileList(dir);
   for (i=0; i<list.length; i++) {
     if (endsWith(list[i], "/"))
       countFiles(""+dir+list[i]);
     else
       count++;
   }
  }
  function processFiles(dir) {
   list = getFileList(dir);
   for (i=0; i<list.length; i++) {
```

```
   if (endsWith(list[i], "/"))
     processFiles(""+dir+list[i]);
   else {
     showProgress(n++, count);
     path = dir+list[i];
     processFile(path);
   }
  }
 }
 function processFile(path) {
   if (endsWith(path, ".tif")) {
//main function
    open(path);
               run("Make Binary");
               run("Analyze Particles...", "size=0-Infinity circularity=0.00-1.00
show=Masks display clear summarize");
               done = sav+"done_"+list[i];
               saveAs("Tiff", done);
   }
 }
```

## 2.6 Conclusions

Nanoporous cerium (IV) oxide membrane was synthesized by anodization of

cerium metal foil followed by calcination of the membrane formed. The anodized cerium

formed a porous membrane, which indicates a useful technique for a variety of

applications including catalysis, fuel cells, and self-cleaning surfaces. The mechanism of

the Ce anodization is proposed to be a balance of cerium oxide formation and dissolution

on the cerium foil surface.

## Chapter 3 – Cerium Oxide Nanorods

### 3.1 Introduction

Nanomaterials of the same compound can vary greatly in their properties. The synthetic method and treatment of the materials can create a wide variety of structures, each with distinct properties. It was determined that a rod like structure could provide a very large surface area that could withstand agglomeration. In addition the rods can be engineered with large areas of single lattice planes. The large surface area could then be engineered to have a wide variety of defects with an emphasis on oxygen vacancy defects. Several methods of creating cerium oxide nanorods were investigated and one was found to reproducibly create rods with the desired properties.[1-2, 11, 17, 69-71]

### 3.2 Materials and Methods

### 3.2.1 General Materials

All water used in this experiment was Ultrapure water of >18 MΩ resistivity and filtered through 0.22 nm pore-sized filters. All chemicals were used as purchased unless otherwise noted. Bulk cerium oxide powder with 300 mesh size (Sigma-Aldrich, St. Louis, MO) and cerium oxide nanoparticles with 7-nm average diameter (Nanoscale, Manhattan, KS) were used for catalytic activity evaluations and comparisons with cerium oxide nanorods. The cerium oxide nanoparticle samples have aggregate particle size $\leq 9$ μm.

### 3.2.2 Synthesis of Cerium Oxide Nanorods

Cerium oxide nanorods were synthesized using a modified method developed by Zhou et al. (Scheme 1) A sample of 0.5 g cerium(III) sulfate hydrate ($Ce_2(SO_4)_3 \cdot X\ H_2O$, Sigma-Aldrich, St. Louis, MO) was first dissolved into 40 mL of 10 M sodium hydroxide aqueous solution (NaOH (aq), Sigma-Aldrich, St. Louis, MO) solution. The solution was transferred to a 45 mL total volume Parr autoclave (Parr Instrument Company, Moline, Illinois). The convection oven in which the autoclaves were placed ramped from room temperature (25 °C) to the reaction temperature of 120 °C where it maintained

temperature for 15 hours while the samples reacted. The convection oven and the autoclaves returned to room temperature in approximately 3 hours after the end of the timer cycle. The cooled sample was filtered using 0.8 μm membranes (Millipore, Billerica, MA) and rinsed with 3 aliquots of 50 mL water. After rinsing, the sample was placed in a convection oven at 50 °C for 1 hour. The samples were then gently powdered using a spatula and heated at 50 °C for an additional hour for this partial oxidation step. The resulting samples were mixed with 50 mL of water, and 50 mL of ~15% hydrogen peroxide ($H_2O_2$, Sigma-Aldrich, St. Louis, MO), immediately followed by sonication for 30 minutes. Following sonication the samples were left in the $H_2O_2$ solution for an additional 60 minutes for their oxidative transformation into tubular structures. Lastly, the material was filtered using a 0.8 μm membrane, rinsed with three aliquots of water and dried in a convection oven at 50 °C.
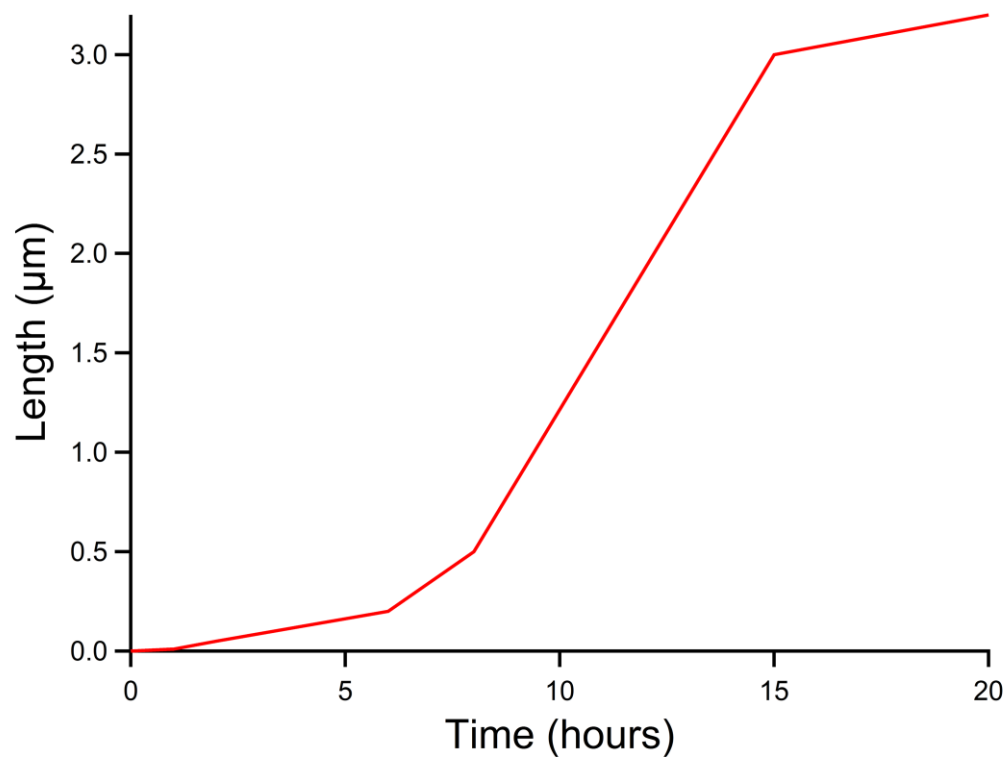
Figure 14 Plot of length of ceria nanowires vs. reaction time of non-hydrogen peroxide treated samples

### 3.2.3 Activation Treatment of Cerium Oxide Samples

Typically, 100 mg of cerium oxide sample (nanoparticles, nanorods or bulk materials) was activated by heating the sample in a 1 inch quartz tube furnace with a 100 SCCM flow of a nitrogen-oxygen mixture (80% $N_2$ and 20% $O_2$) for 1 hour at 350 °C under vacuum with an operating pressure of 0.1 Torr. Control samples were activated using similar experimental condition but with 1 atmosphere operation pressure.

### 3.3 Nanorod Growth Mechanism

Evidence presented by TEM studies of nanorods indicates nanorod/tube growth is anisotropic and likely due to screw dislocations.[42, 72-74] The diameter of the nanorods are consistently 20 nm, but the length prior to sonication increases with time (Figure 14) that the reaction mixture is maintained at reaction temperature. After 2 hours the nanorods are only a few tens of nm long, after 6 hours the nanorods are becoming more wire-like and are up to 100 nm long, after the full 15 hours the nanowires are as long as one µm. After 15 hours there is little evidence of continued lengthening.

Dislocation-driven anisotropic crystal growth is the preferred growth due to self-perpetuating spirals of axial screw dislocations under conditions of low super saturation. According to the Burton-Cabrera-Frank (BCF) theory, as super saturation increases the growth mechanism changes from dislocation growth, to layer-by-layer growth (LBL), and dendritic growth.[75] Therefore, based on the very low super saturation of $Ce_2(SO_4)_3$, it is likely that the growth mechanism is by screw dislocation.

**3.4 Formation of a High Density of Defects on the Nanorods**

The formation of highly defective nanorods was desired for this research. A series of rapid oxidation steps, and Kirkendall diffusion with hydrogen peroxide was used to increase the density of grain and lattice defects present on the surface (Figure 15). The as-synthesized cerium (III) hydroxide ($Ce(OH)_3$) nanorods and nanowires were subjected to rapid oxidation at 50 °C in a convection oven. This rapid oxidation led to the formation of a core-shell material with cerium oxide ($CeO_{2-x}$) forming a hard outer shell of the cubic fluorite structure and the core remains $Ce(OH)_3$ in the simple hexagonal structure. The rapid conversion between the two crystalline structures led to myriad defects on the surface. This material was then sonicated in hydrogen peroxide ($H_2O_2$) leading to the cracking of the materials and the more rapid diffusion of the $Ce(OH)_3$ away from the core rather than $CeO_{2-x}$ away from the shell.

Ce$_2$(SO$_4$)$_3$ + NaOH

Hydrothermal
Synthesis

= Ce(OH)$_3$

= Ce$_2$O$_3$ / CeO$_2$

= CeO$_2$

Air
Δ

HAuCl$_4$

H$_2$O$_2$

Air
Δ
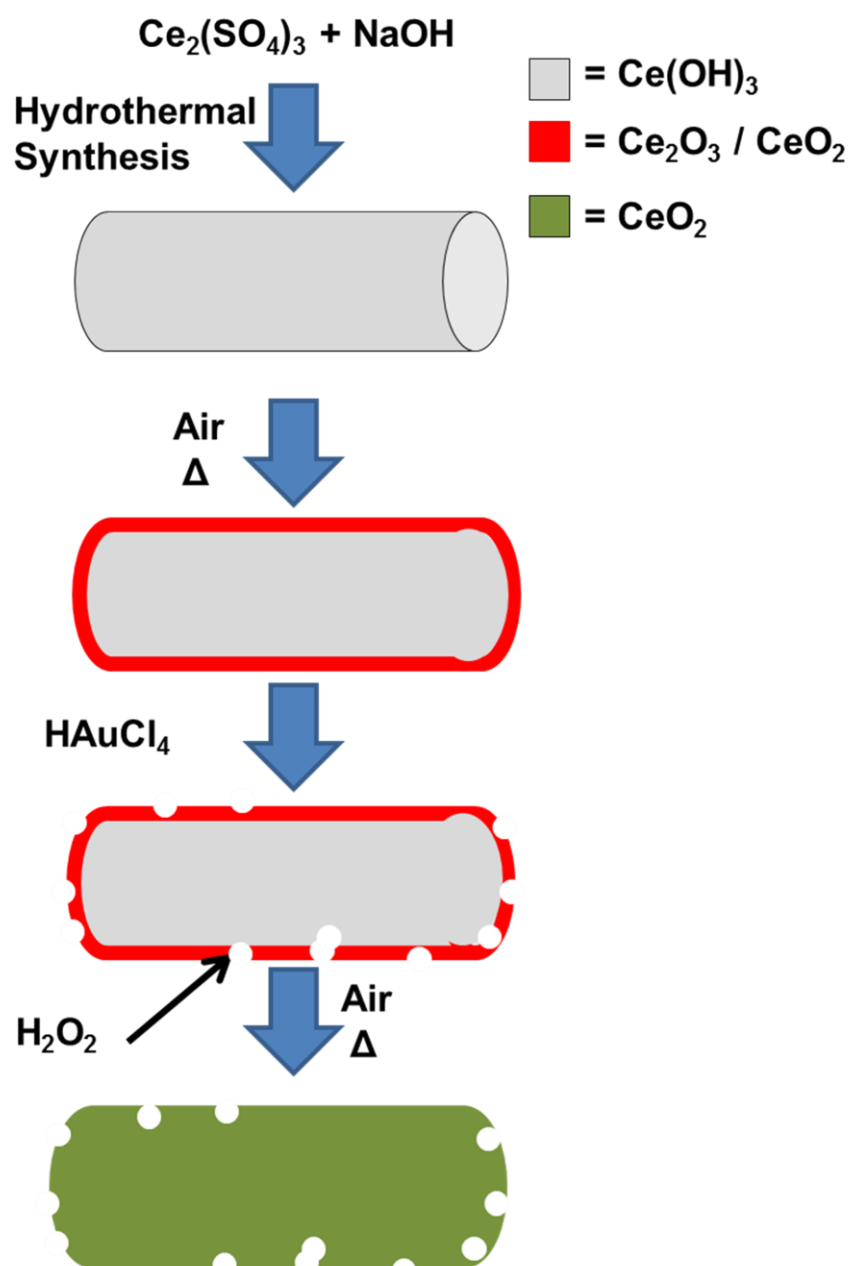
Figure 15 Schematic mechanism for the formation of nanorods by Kirkendall

diffusion

The $H_2O_2$ acts as oxidant for $Ce^{3+}$. The $Ce^{3+}$ ions present in the $Ce(OH)_3$ nanorods can be converted to a $Ce^{4+}$ complex, $Ce(OH)_2^{2+}$, by hydroxyl free radicals in the hydrogen peroxide solution:

$$2Ce_{(S)}^{3+} + 2OH^- + H_2O_2 \longrightarrow 2Ce(OH)_2^{2+} \tag{1.1}$$
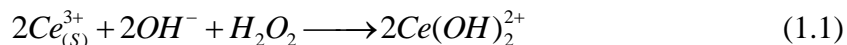
thus, the $Ce(OH)_2^{2+}$ transfer into the solution. As the concentration of the $Ce(OH)_2^{2+}$ increases, ceria can be formed easily under the following reaction:

$$Ce(OH)_{2(aq)}^{2+} + 2OH^- \longrightarrow CeO_{2(s)} + 2H_2O \tag{1.2}$$
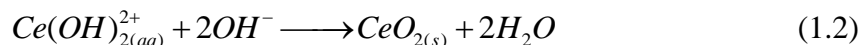
## 3.5 Nanorods Characterization Chemical Composition, Surface, and Valency

### 3.5.1 Composition

Testing with both energy dispersive X-ray spectroscopy (EDX), Figure 16 and with X-ray photoelectron spectroscopy (XPS) (Figure 18, Figure 19, Figure 20 and Figure 21) demonstrate that cerium oxide materials were all of the formula $CeO_{2-x}$ where x accounts for the ratio of $Ce^{3+}$ in the lattice. All samples tested were found to have and to retain the cubic fluorite structure of $CeO_2$ [space group Fm3m (No. 225); joint committee on powder diffraction standards JCPDS card 34-0394] leading to the initial conclusion that any $Ce^{3+}$ found must be at or near the surface, as this is the most common location for the formation of OVDs. After calcination no evidence of $Ce(OH)_3$ (JCPDS card 74-0665) remained in the XRD spectra.
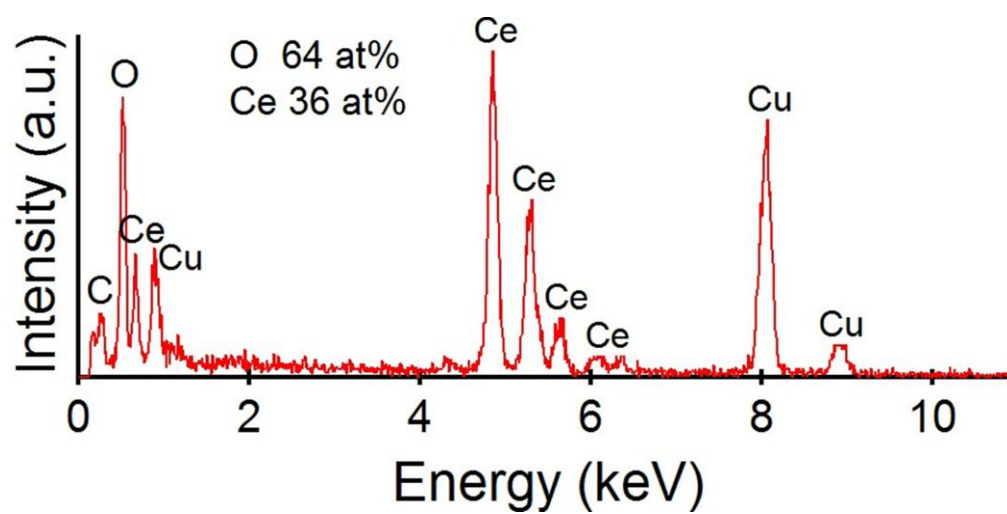
Figure 16 EDX spectrum of CeO$_{2-x}$ nanorods

### 3.5.2 Surface Area

The surface areas of the three types of cerium oxide catalysts (bulk powder, nanoparticles, and nanorods) was determined via the Braunauer Emmet Teller (BET) extension of the Langmuir isotherm with a Micromeritics ASAP 2010 (Micromeritics, City, ST).[76] Nitrogen was used as the adsorbent gas in these experiments.

### 3.5.3 Surface Defects

The structural morphology of the cerium oxide samples was examined with a field emission scanning electron microscope (FE-SEM, Hitachi S4700, Hitachi High Technologies America, Inc. Pleasanton, CA) operated at 15keV. Detailed structures of nanomaterials were investigated by high resolution transmission electron microscopy (HRTEM) with a Tecnai G2 F20 S-Twin operated at 200keV (FEI, Hillsboro OR). Selected area electron diffraction (SAED) was used to determine the local structures of the materials. Each TEM sample was prepared by drop-casting a solution of sample sonicated, for no more than 5 seconds, in methanol onto a holey carbon film on a copper grid support. X-ray diffraction (XRD) of the samples was performed with a Bruker AXS D8 Discover equipped with a GADDS area (Bruker AXS Inc. Madison, WI) to examine the crystallinity and crystal structure of the samples in bulk form. The weighted average wavelength of the Cu K$\alpha$ x-ray sourcewas1.5417 Å. (Figure 17)
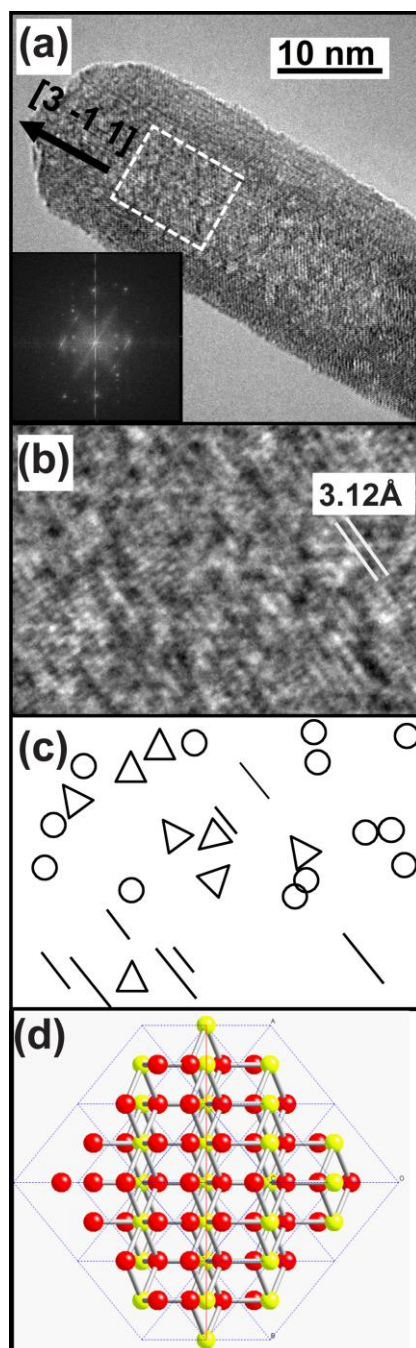
Figure 17 Microscopic images of (11-2) focal plane surface defects on an activated CeO$_{2-x}$ nanorod. Showing a) nanorod with enlarged area highlighted and showing rod growth direction. Inset is SAED of this area. b) enlargement of the highlighted area for easier viewing of the defective surface. And c) a map highlighting some of the surface, subsurface and linear defects. Finally d) is a simulation of the focal plane from which this image was taken to show (111) lattice fring spacing and (3-11) growth direction.
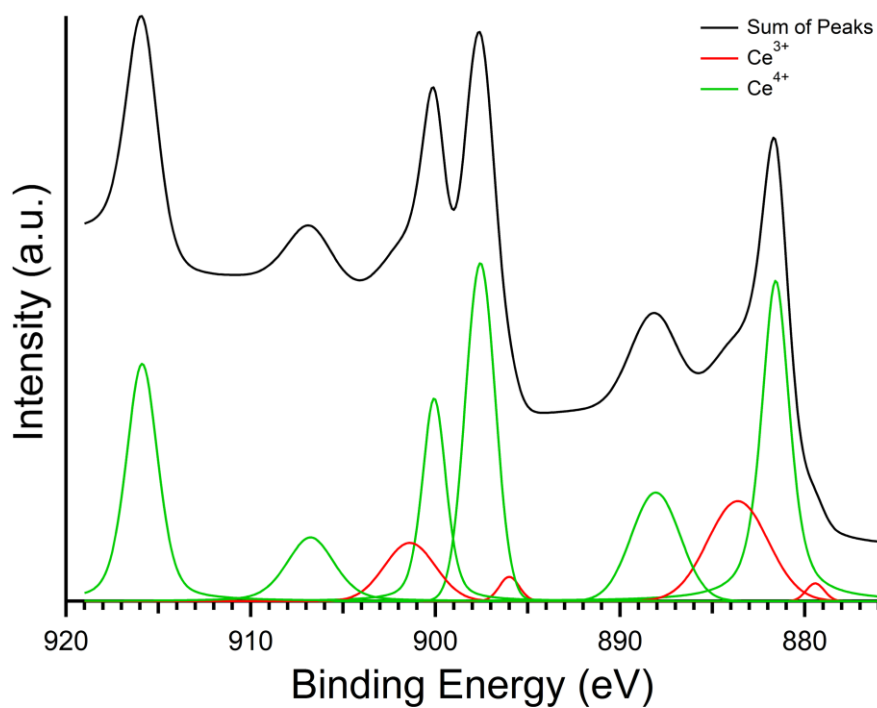
Figure 18 Curve fix of XPS spectra of bulk $CeO_2$ before activation showing sum of peaks
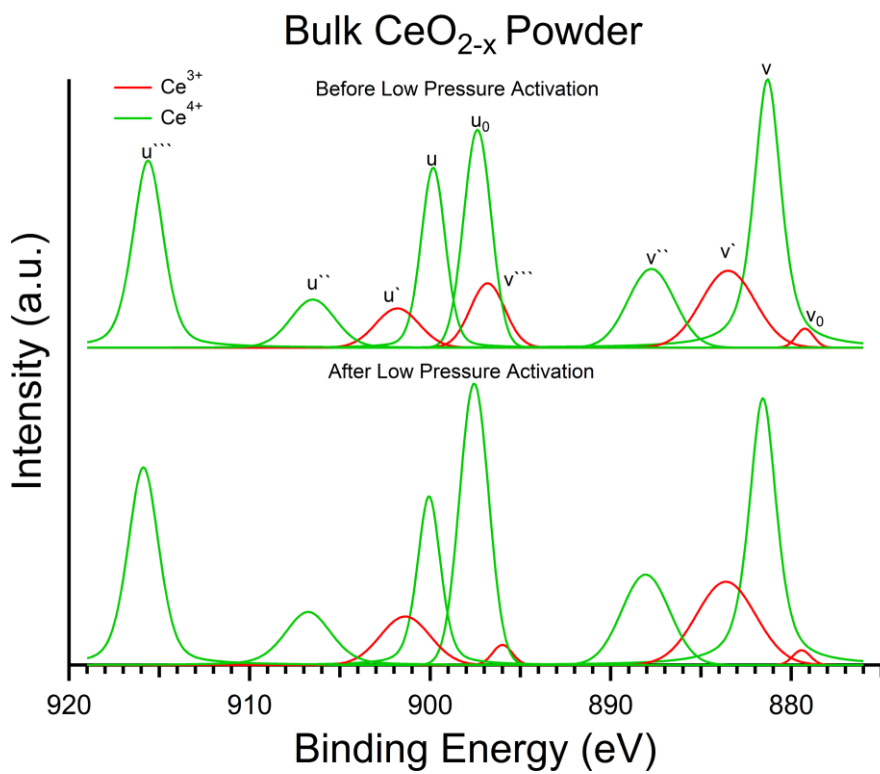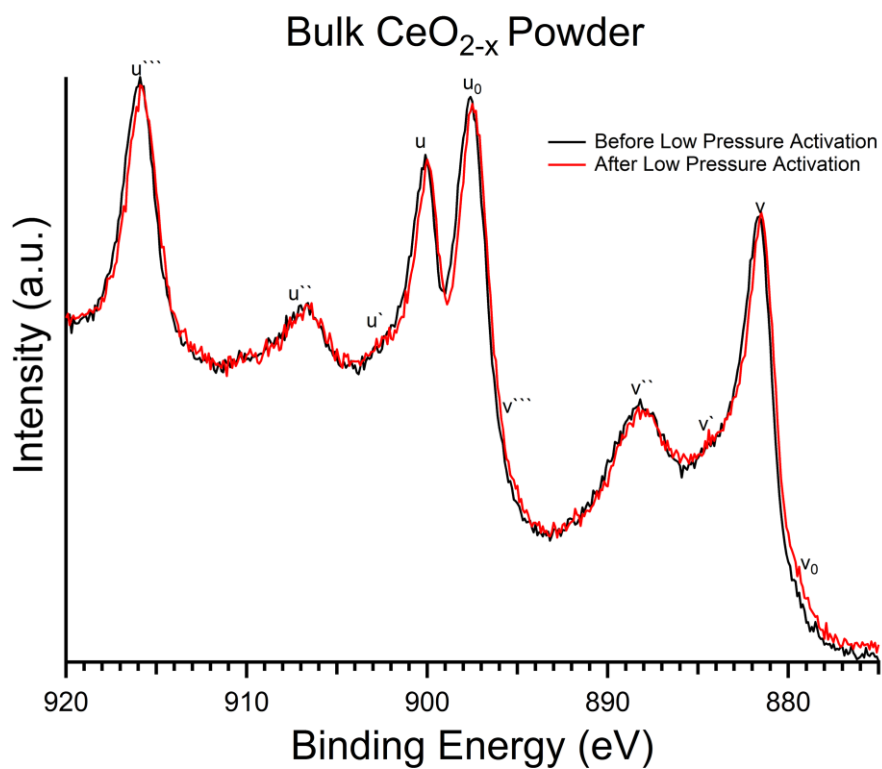
Figure 19 XPS spectra of bulk CeO₂ before and after activation showing
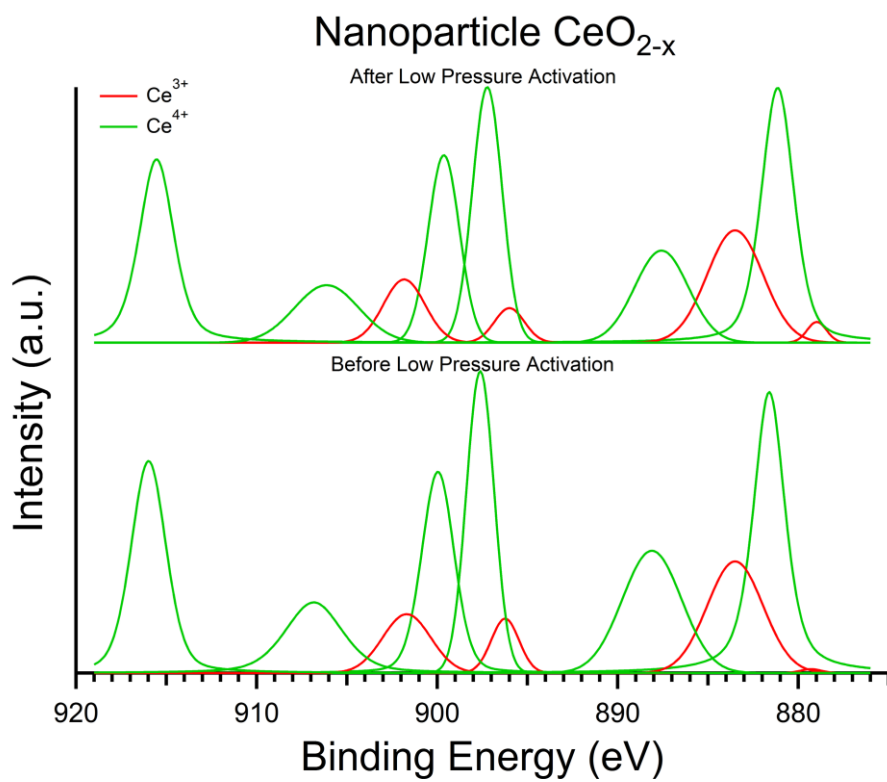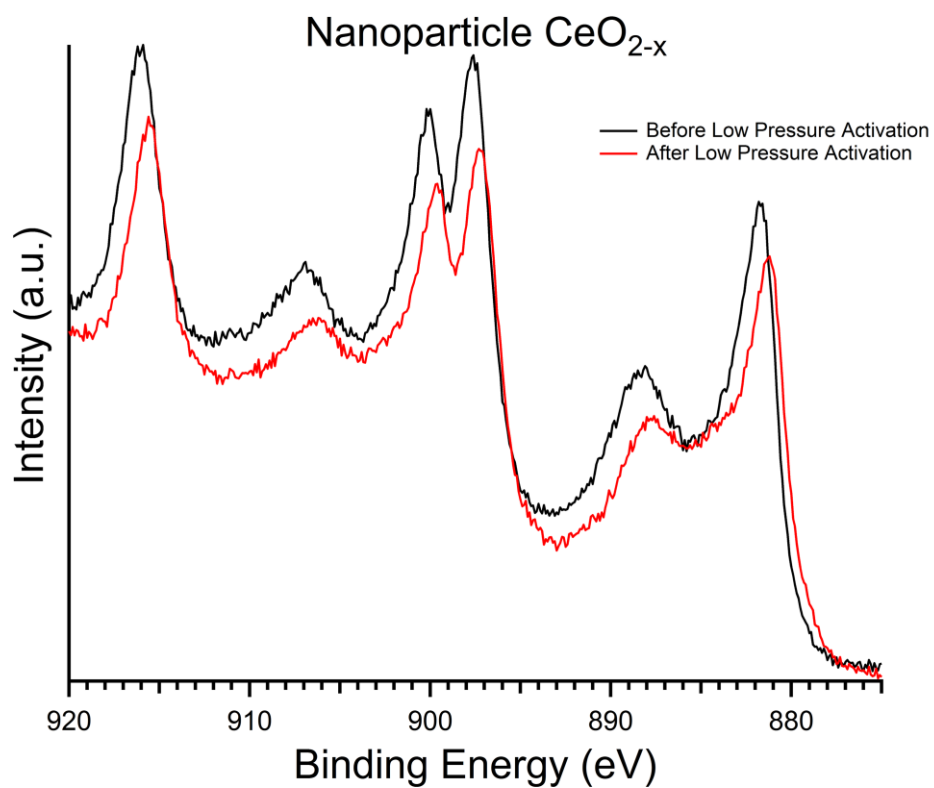
Figure 20 XPS spectra of CeO₂ nanoparticle before and after activation
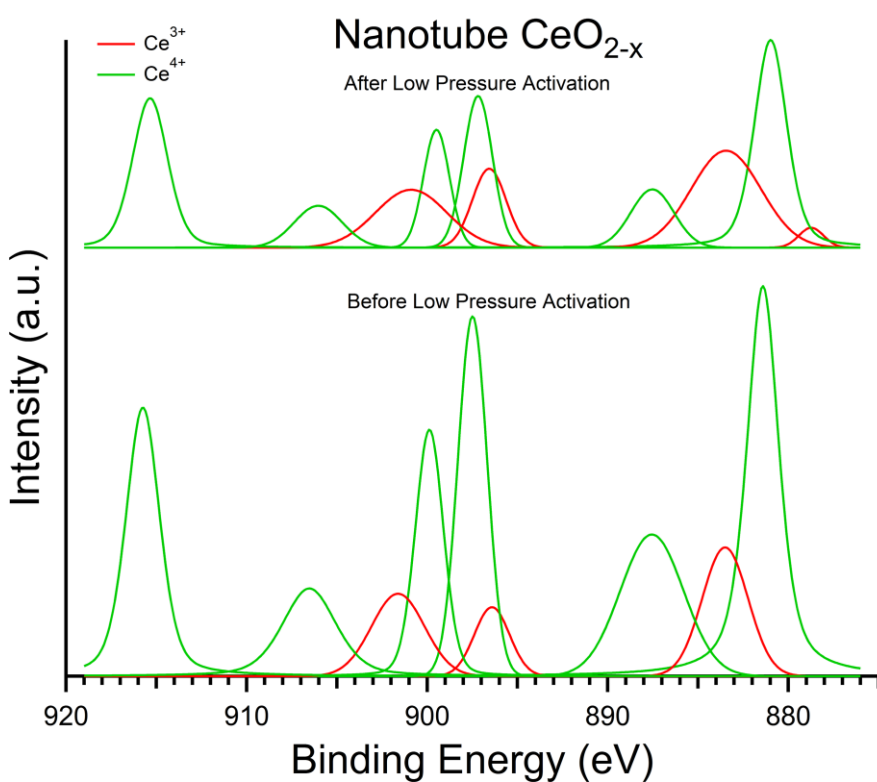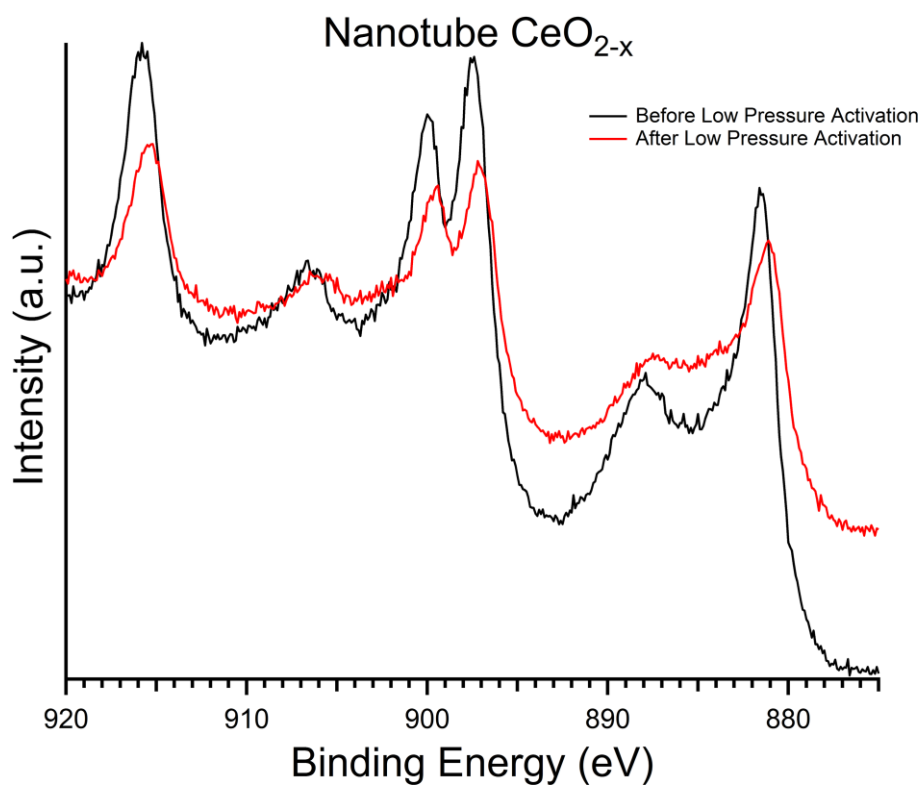
Figure 21 XPS spectra of nanorod CeO$_2$ before and after activation

**3.5.4 Valency of Cerium**

The $Ce^{3+}/Ce^{4+}$ ratio for each sample was quantified by XPS (VersaProbe™ Scanning XPS Microprobe) according to recent literature. XPSpeak 4.1 for Win 95/98 [77] was used to subtract a fitted base line using the Shirley algorithm from the data, no linearization was assumed and the baseline was expected to encompass the entire spectrum. The Shirley algorithm is used as a least incorrect baseline method optimized to remove as much asymmetry as possible from the baseline data. Semi-Voigt functions (convolved Gaussian-Lorentzian line shapes) were then fitted to the resulting spectrum to determine the area of each of the ten peaks corresponding to the signals from $Ce^{3+}$ and $Ce^{4+}$. The peaks were fitted in a series of iterations, which allowed the areas and their full width at half maximum to vary throughout all steps. The percentage of Gaussian contribution for each line shape was allowed to vary between 80 and 100% after the initial fit. The peak location was allowed to vary up to 0.2 eV due to the nanoscale nature of the materials during the last iteration.[78-79] The ratio of the integrated peak area was then calculated as indicated in eq. (1.3) by comparing the peak areas for $Ce^{3+}$ to the total area calculated for both $Ce^{3+}$ and $Ce^{4+}$ according to the reported literature.[48, 79]

$$\% Ce^{3+} = \left( \frac{[A_{v0} + A_{v'} + A_{u0} + A_{u'}]}{[A_{v0} + A_{v} + A_{v'} + A_{v''} + A_{v'''} + A_{u0} + A_{u} + A_{u'} + A_{u''} + A_{u'''}]} \right) * 100\% \qquad (1.3)$$

There are two concerns about the XPS data method of analysis. First, the x-ray source creates a core hole in the $3d$ band which in turn leads to a rearrangement of the electron energy leading to a change in the hybridization of the oxygen $2p$ and the cerium $4f$, making it appear that the cerium is in the $4f^{1}$ state rather than the $4f^{0}$, which will add to the complexity of the analysis of the peaks. As long as all ten peaks are integrated, this

problem can be overcome.[80-81] Second, XPS is necessarily done under high vacuum conditions; it has been shown that under low pressure conditions $CeO_2$ will reduce to form $Ce_2O_3$. Therefore if the spectra are not recorded quickly the ratio of $Ce^{3+}$ to $Ce^{4+}$ will have changed. However, careful studies have been done with good results being reported of natural ratios between 17 and 25 at.% which corresponds well to the increase of OVD sites due to increased surface energy.[48, 79, 82-83] This naturally calls into question the stability (Table 2) of the materials when they are in an artificially high ratio of $Ce^{3+}$ to $Ce^{4+}$.

## 3.6 Effects of Catalyst Activation by Thermal Annealing

### 3.6.1 Changes in $Ce^{3+}$ to $Ce^{4+}$ Valence Ratio

By utilizing XPS the atomic ratio for the as-synthesized nanorods was found to be 16% $Ce^{3+}$ while the ratio for the nanoparticles and bulk ceria were found to be 25% for both. The high percentage of $Ce^{3+}$ found in the bulk material is likely accounted for by the micron scale of the powder particulates. The atomic ratio of $Ce^{3+}$ did not change for any of the samples when activated under standard pressure at 400 °C. When the samples were activated at 400 °C and 0.1 Torr, the atomic ratio of $Ce^{3+}$ increased for both the nanorods and the nanoparticles to 39 and 36 % respectively, but did not change for the bulk material. The increase in $Ce^{3+}$ is likely due to a change in the partial pressure of the system, Figure 3 encouraging the desorption of oxygen from the surface of the materials. In the bulk material, the oxygen storage capacity of the cerium oxide was probably able to buffer the small amount of oxygen desorbing from the surface. Additionally the total surface area exposed to the low pressure is certain to be a factor in the amount of change

in the $Ce^{3+}$ ratio as demonstrated by the more significant change experienced by the nanorods over the nanoparticles.

Both of the nanoscale materials (nanorods and nanoparticles) were found to have significantly elevated ratios of $Ce^{3+}$. The elevated ratios of $Ce^{3+}$ were stable for more than a week, as demonstrated by XPS, and long term catalytic data presented in chapter four.

There must be a stabilizing effect that is occurring at or near the surface of the nanomaterials, since the materials have demonstrated to be pure by EDX Figure 16. Since they have no significant amounts of impurities we can begin to look at the activation process. It is suspected that during calcination OVD are formed due to the low partial pressure leading to the equilibrium driven formation of $O_2$. These defects are of higher energy than the well-defined sites and therefore are more likely to form initially near locations where they can be stabilized. These stabilization locations are likely to be surface defects of the lattice since at these points the energy is much higher and therefore would be able to stabilize the OVDs, lowering the energy of the surface defect.[21, 56, 84] The surface defects, once exposed to atmospheric conditions, are then likely to react with $CO_2$ to form trace amounts of cerium carbonates ($Ce_2(CO_3)_3$ and $Ce_2(CO_3)_4$) below the detection limits of our equipment. Cerium carbonate is a very stable compound with little catalytic activity. However the presence of a very small amount of cerium carbonate on the surface of the nanomaterials is likely enough to stabilize the $Ce^{3+}$ that are a part of OVD sites.

| CeO$_{2-x}$ Sample | Ce$^{3+}$/Ce$^{4+}$ at.% Activation Before | After | TON @250 °C μmol*g$^{-1}$*sec$^{-1}$ | Surface Area m$^2$/g |
|---|---|---|---|---|
| nanorod | 16 | 39 | 2.21 | 113 |
| Nanoparticle | 25 | 36 | 0.22 | 50 |
| Area adj. | | | .993 | |
| Bulk | 25 | 25 | 0.01 | 8 |

Table 2 comparison of valence ratio and surface area of CeO$_{2-x}$ materials activated at ambient and low pressure

### 3.6.2 Changes in Defect Sites

Utilizing HRTEM we were able to identify a variety of defects.[37, 61] Most interestingly we were able to identify the formation and increase in density of oxygen vacancy defects (OVD). (Figure 17) The presence of increased OVD after activation and the subsequent stability of the OVD after a reaction lead us to the conclusion that the low pressure activation is creating these defect sites.

### 3.7 Conclusions

During activation, various vacancy cluster defects were added to the surface and subsurface of the materials. The addition of these defects to the ceria nanorods led to enhanced catalytic activity of the nanorods with respect to other nanoparticles synthesized in a similar fashion, or of similar structure. This increases our understanding of the importance of both types of defects for the studied materials.

The identification of vacancy clusters using HRTEM proved promising, as many of these types of defects were identifiable utilizing this method. The ability to identify OVDs using HRTEM rather than STEM makes the identification of these defects accessible to more research groups. Step edge and grain boundary defects were introduced into the ceria nanorods during synthesis.

## Chapter 4 - Catalytic Oxidation of Carbon Monoxide

### 4.1 Introduction

The invention and subsequent popularity of the automobile lead to a need to convert the emissions to more benign substances.[14, 21, 85-87] This was the impetus behind the three way catalyst. As the name implies three way catalysis is the catalytic conversion of three different materials simultaneously. First, any carbon monoxide CO must be fully combusted into carbon dioxide $CO_2$. Second, any unburned hydrocarbons $C_xH_y$ must be oxidized to $CO_2$ and water. Third any oxides of nitrogen $NO_x$ need to be reduced to nitrogen gas $N_2$. It seems intuitive that the combustion of CO and hydrocarbons can be done under the same conditions; however, the reduction of $NO_x$ at first appears to require its own set of conditions and possibly a separate catalyst. When it is considered that $NO_x$ needs to be reduced and that CO is a very good reducing agent the solution becomes clear: a location is needed to store excess oxygen from the $NO_x$ while awaiting CO. This location is on the surface of the cerium oxide.

### 4.2 Catalytic Oxidation

Combustion, when it occurs on a cerium oxide catalyst, has two major advantages over flame combustion. First, the radicals, which are produced as an intermediate in the reaction, are constrained to the surface of the cerium oxide and maintained there until needed for further reaction. The reaction is limited by kinetics rather than the mass transport limitations of flame combustion.[88-91] This allows the reaction to occur at much lower temperatures than exist in a flame (between 1100 and 1800 °C), which in many cases is desirable. Second, the formation of byproducts is greatly reduced due to the

alternative reaction path provided by the cerium oxide surface. This leads to very

predictable products and therefore a cleaner effluent.

## 4.3 Lite Off Number and Turn Over Number

Currently the state of the art in the production of heterogeneous catalysts is

measured through two primary numbers. First the turn over number (TON), also called

the turn over frequency (TOF), is a measure of the number of micromoles of carbon

monoxide per second per gram of catalyst ($\mu mol*g^{-1}*sec^{-1}$) reported at a given

temperature that is oxidized to carbon dioxide.[92] This is a measure of the rate of reaction.

The second number is the light-off number ($T_{50}$), the temperature at which a given

amount of catalyst can oxidize fifty percent of the carbon monoxide flowing through it.

The $T_{50}$ is a measure of the reduction in the activation energy of the reaction by a given

catalyst. (Figure 23)

## 4.3.1 Energy of Activation

The apparent change in the energy of activation (Ea) can be approximated using

the Arrhenius equation

$$k(T) = ve^{-Ea/RT}$$

where k is the rate constant, T is the temperature in Kelvin, v is the pre-exponential

factor, and R is the ideal gas constant. The equation is rearranged giving

$$\ln k(T) = \ln v - \frac{Ea}{R}\frac{1}{T}$$

According to this equation the slope of the plot yields the activation energy and the intercept yields the pre-exponential factor. The plot must be at the temperatures nearest to the lite off temperature in order to have physical meaning.[7]

Several assumptions must be made when using this technique to calculate the apparent change in Ea. It is assumed that the rate limiting elementary reaction is first order, and one of the reactants is limiting. In a catalytic reaction, it is assumed that the substrates are in great excess to the reaction sites on the catalyst. It was also assumed that the apparent Ea is valid throughout the entire range plotted. Finally, it is assumed that k(T) can be written as $k(T) = ve^{-Ea/RT}$. When graphing the Arrhenius plots for these reactions (Figure 22), the chosen temperature range was selected from onset to $T_{50}$.
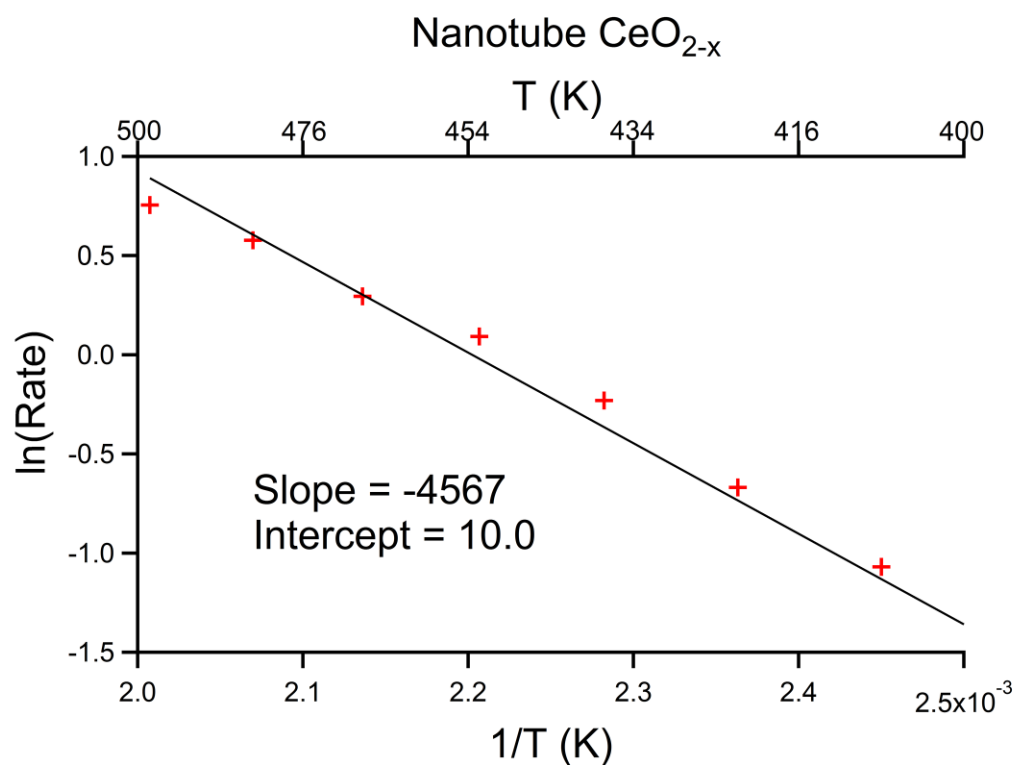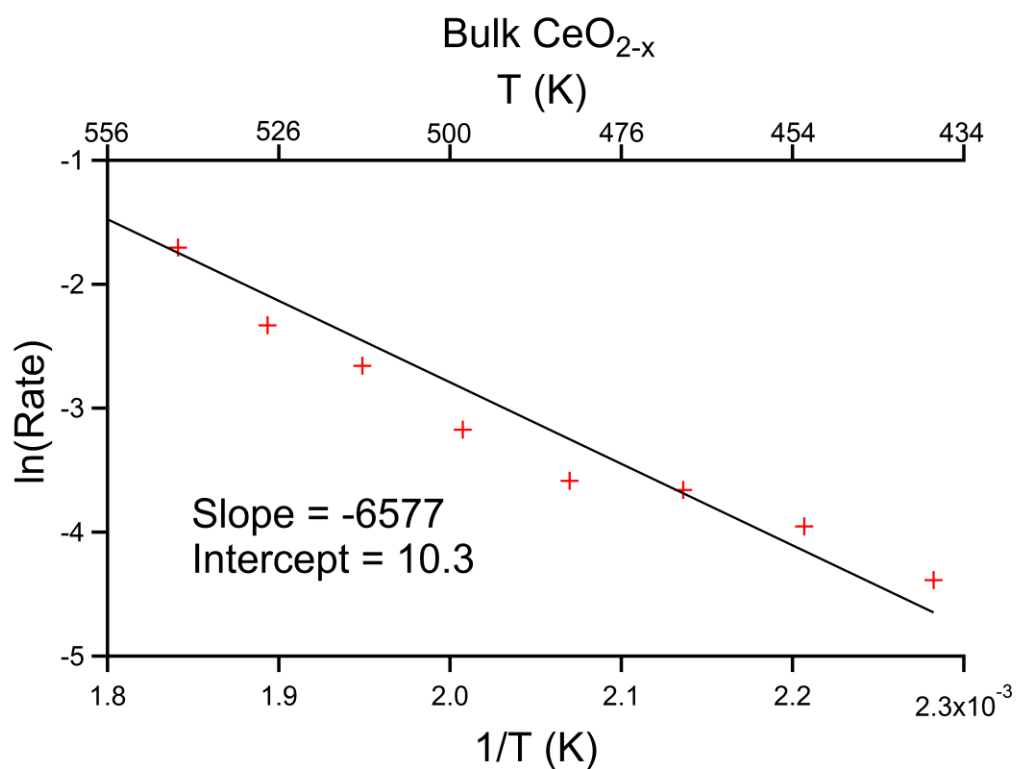
Figure 22 Arrhenius plots for ln(k) vs 1/T

**4.4 Materials and Methods**

**4.4.1 Materials**

Quantified mixtures of CO (1.08 % v/v) $O_2$ (20.1% v/v) with the balance He (Linweld, Lincoln NE) was used for the reaction precursors. $CO_2$ (1.98% v/v) in He (Linweld, Lincoln NE) was used to calibrate the GC and column under a variety of conditions.

**4.4.2 Reactor Design**

A stationary catalyst bed was selected due to the volume of catalyst and reactants that were to be tested. Thirty SCCM CO and $O_2$ in a He balance were flowed from storage through a mass flow controller (MFC), into a 1 cm diamater U shaped reactor with a coarse-grained quartz frit sample platform located in one of the legs of the reactor also known as a plug flow reactor. The system was designed such that a quartz sheathed thermocouple was in contact with the frit and the reactor bed. The U micro-reactor was located in an open ended furnace capable of temperature control from room temperature to 500 °C. Downstream from the micro-reactor the gases entered a GC through a 6 port valve to allow for continuous filling of the sample loop. Exhaust gasses were expelled through a bubbler to allow for monitoring of gas flow in the system. All connectors were either Swagelok® or Ultra-Torr®. To provide for a gas tight configuration, Ultra-Torr® fittings were used wherever regular disconnections were needed. Tubing bends and bend angles were kept to a minimum to prevent changes to the conductance of the gas. 1/8" Stainless steel tubing was chosen as the primary tubing for the system. He carrier gas for the GC was conducted through 1/4" copper tubing.

### 4.4.3 Reactor Conditions

Typically, in each catalysis test, a mixture of 79 % He, 20 % $O_2$ and 1 % CO was flowed continuously throughout the reaction at a rate of 30 SCCM through a 100-mg $CeO_{2-x}$ sample, completely covering the frit. For our reaction gas mixture of 1.08 % CO this equates to 2.21 $\mu mol*g^{-1}*sec^{-1}$, assuming 25 °C and 1atm pressure at the MFC, giving us an upper bound for our conversion rate

$$n = \frac{pV}{RT} = \frac{1atm*0.030\,L/min}{0.082057\dfrac{L\,atm}{mol\,K}*298K} = 1.226*10^{-2}\frac{mol}{min} = 204.3\frac{\mu mol}{sec}\,total\,gas$$

$$\left(\frac{204.3\dfrac{\mu mol}{sec}\,total\,gas}{0.1\,g\,CeO_2}\right)1.08\%\,CO = 2.1\frac{\mu mol\,CO}{g*sec} \tag{1.1}$$

The reaction chamber was warmed in 5 °C increments from room temperature to 300 °C or until at least 20 °C past the 100% conversion temperature.

A 1 mL sample of process gas obtained at each reaction temperature was analyzed using a gas chromatography instrument (Gow-Mac, Bethlehem, PA), equipped with an eight foot porapak Q column (Waters Corp., Milford, MA) and a thermo conductivity detector (TCD). The percentage of CO conversion was determined by quantifying the carbon dioxide concentration in the processed gas compared to a known concentration of $CO_2$ in helium. The GC conditions were originally set to those specified by the column manufacturer and were modified slightly to enhance performance. The original conditions were: inlet temperature of 100 °C, oven temperature of 60 °C, detector temperature of 100 °C, detector current of 100 mV and a carrier gas flow of 20 SCCM. These were modified to an oven temperature of 80 °C, detector temperature of 110 °C

and detector current of 150 mV. The increased oven temperature increased the elution time through the column, which given the purity of our mixture still allowed for baseline separation. The increased detector temperature and current allowed us to increase the sensitivity of the detector.

## 4.5 Results and Discussion

### 4.5.1 Change in the energy of activation

The light off temperature ($T_{50}$) was used as a comparison of the catalytic activity of each of the cerium oxide materials tested. A comparison of the tested materials along with various literature values is reported in Table 3. As controls, materials were activated at 400 °C at ambient pressure. The $T_{50}$ for nanorods, nanoparticles and bulk cerium oxide were found to be 205, 285, and 350 °C respectively. The $T_{50}$ showed that both the nanorods and the nanoparticles were more active after activation at 0.1 Torr than when activated at ambient pressure, additionally the nanorods were more active than the nanoparticles with a $T_{50}$ of 175 and 260 °C respectively. The turn over number (TON) at 250 °C for low pressure activated nanorods, nanoparticles, and bulk cerium oxide (Table 3) were 1.77 $\mu mol*g^{-1}*sec^{-1}$, 0.22 $\mu mol*g^{-1}*sec^{-1}$, and 0.01 $\mu mol*g^{-1}*sec^{-1}$ respectively.

When the natural log of the rate was plotted versus 1/T (Figure 22) for the bulk cerium oxide the pre-exponential factor was determined to be 10.3 and the apparent energy of activation over R ($\frac{-Ea}{R}$) was calculated to be 6.577 J/mol. The calculated pre-exponential value for low pressure activated nanorods was determined to be 10.0 with an apparent energy of activation over R calculated to be 4.567 J/mol. The units of the pre-exponential factor and apparent energy of activation are arbitrary without further

investigation into the order of the reaction. However even without an exact knowledge of the units, it is apparent that there is a distinct lowering of the apparent energy of activation for the reaction when it is catalyzed by low pressure activated nanorods vs. low pressure activated bulk cerium oxide powder.

### 4.5.2 Comparison to Literature Data

The reported values of $T_{50}$ for pure ceria range from 175 to 350 °C, our material $T_{50}$ is reported at 175 °C. The reported TON for pure ceria ranges from 0.01 to 3.2 $\mu mol*g^{-1}*sec^{-1}$ @ 250 °C with our material being reported at 2.21 $\mu mol*g^{-1}*sec^{-1}$ @ 250 °C. See Table 3 for a detailed comparison.

### 4.5.3 Long term catalytic stability

It was determined that after 96 hours of continuous reaction at 170 °C there was no change in the catalytic activity of the low pressure activated nanorods. The long term stability of the reduced state of the cerium oxide was unexpected; we anticipated that after a catalytic run, especially a week long run, the majority of the cerium would have returned to the $Ce^{4+}$ state. There must be a stabilizing effect that is occurring at or near the surface of the nanomaterials. The materials have demonstrated via EDX to be pure and since they have no significant amounts of impurities therefore the difference must be related to the activation process.

### 4.5.4 Increased $Ce^{3+}/Ce^{4+}$ ratio

All samples tested were found to have and to retain the cubic fluorite structure of $CeO_2$ this leads us to the initial conclusion that any $Ce^{3+}$ found must be at or near the surface as this is the most common location for the formation of OVDs. The relatively

low surface area for the nanoparticles was due to tightly agglomerated micron sized particles.

Both of the nanoscale materials (nanorods and nanoparticles) were found to have significantly elevated ratios of $Ce^{3+}$ after activation. Because the samples are activated at low pressure under flowing nitrogen and oxygen rather than compressed air, it is suspected that during calcination the oxygen vacancy defects are formed. These defects are of higher energy than the well-defined sites and therefore are more likely to form initially near locations where they can be stabilized. These stabilization locations are likely to be surface defects of the lattice. At these points the energy is much higher and therefore would be able to stabilize the OVDs lowering the energy of the surface defect. The surface defects, once exposed to atmospheric conditions, are likely to react with $CO_2$ to form trace amounts of carbonates of cerium ($Ce_2(CO_3)_3$ and $Ce_2(CO_3)_4$) below the detection limits of our equipment. Cerium carbonate is a very stable compound with little catalytic activity; however the presence of a very small amount of cerium carbonate on the surface of the nanomaterials is likely to stabilize the $Ce^{3+}$ in the oxygen vacancy defects.
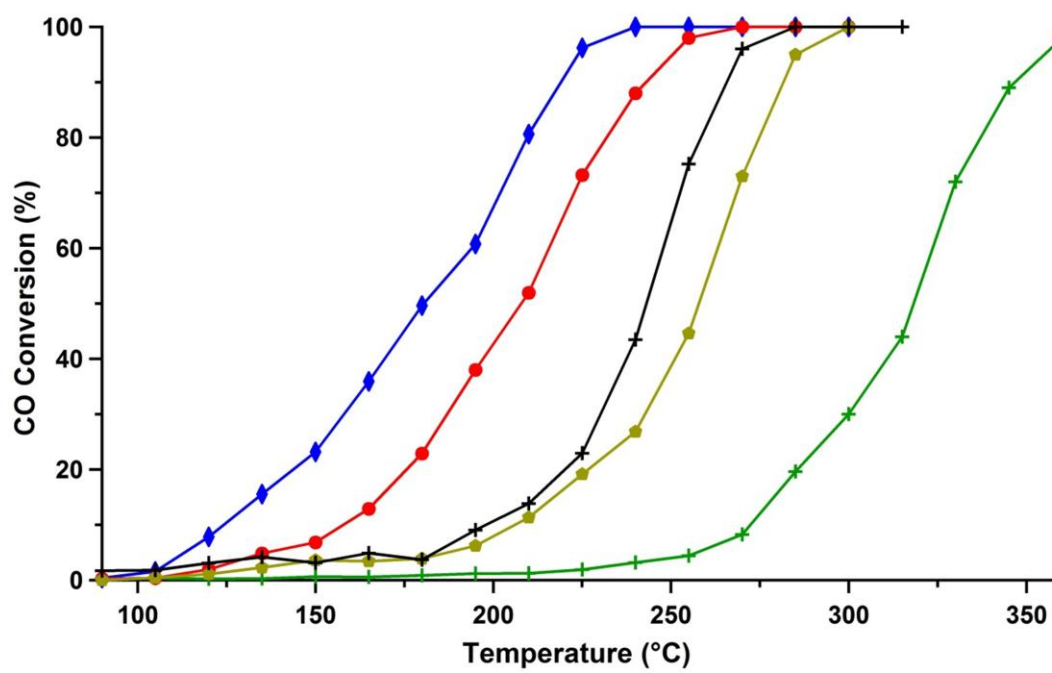
Figure 23 Comparison of changes in $T_{50}$ for nanorods, nanoparticles, and bulk powder ceria

**4.6 Conclusions**

During activation various vacancy cluster defects were created on the surface and subsurface of the materials. The addition of these defects to the ceria nanorods led to enhanced catalytic activity of the nanorods with respect to other nanoparticles synthesized in a similar fashion, or of similar structure. This increases our understanding of the importance of both types of defects for the studied materials.

The identification of vacancy clusters with HRTEM proved promising as many of these types of defects were identifiable utilizing this method. The ability to identify OVD clusters using HRTEM rather than STEM makes the identification of these defects accessible to more research groups.

| Shape | TON (µmol g-1 sec -1) | T$_{50}$ (°C) | Reference |
|---|---|---|---|
| Bulk | 0.01 | 350 | This thesis |
| | Not reported | 290 | [1] |
| Nano rod | 2.21 | 175 | This thesis |
| | 2.21 | 205 | This thesis |
| | 1.81 | 223 | [2] |
| | 2.272 | 250 | [3] |
| | 1.79 | 224 | [2] |
| | 1.13 | 290 | [4] |
| Nano cube | 0.655 | 315 | [2] |
| | 0.055 | 375 | [5] |
| Nano wire | 1.63 | 245 | [2] |
| Shuttle | 3.181 | 160 | [4, 6] |
| Flower like | 0.409 | 325 | [5] |
| | 0.341 | 350 | [5] |
| Nano active™ | 0.993 | 260 | This thesis |
| | 0.860 | 285 | This thesis |
| Nano cube (hollow) | Not reported | 265 | [10] |
| Nano tube | Not reported | 200 | [11-13] |
| Nano tube | Not reported | 200 | [11] |
| Nano tube (L) | Not reported | 270 | [1, 14] |
| Nano tube (T) | Not reported | 270 | [1] |

Table 3 Comparison of reported data for cerium oxide similar in size and shape to those tested in this thesis.

When not reported or reported at temperatures other than 250 °C every attempt was made to calculate the information from the reported data.

# Chapter 5 – Future Work

There is much work left to be done to understand the scientific principles behind multivalent metal oxide catalysis. Ceria will likely be increasingly used for its catalytic properties in a variety of applications and conditions. It is important to remember that there is no "one size fits all" approach to catalysis. For some applications, a lower $T_{50}$ may be required, while others a thermal stability may be of higher priority. To this end we need to be able to correctly model and synthesize catalysts that have very exacting properties.

Using different sample preparations and the interaction of metal atoms with the mixed valency ceria cleverly designed catalysts will soon be more readily available. Ceria catalysts decorated with gold or other noble metal atoms can greatly increase the turn over number. Also, binary metal oxides have been shown to have very interesting catalytic properties while enhancing stability. Finally multilayer catalysts may be able to catalyze a series of reactions. Some work has been done to progress the goal of designer catalysts, but little work has focused on the principles behind the enhancements until the work presented here.

## 5.1 Porous Cerium Oxide Membranes

The ceria membranes should be tested in prototype solid oxide fuel cells. These can be created utilizing off-the-shelf test cells and inserting our membrane into the reaction chamber. The conditions for the reaction are likely between 600 and 1000°C. These conditions should be able to be modulated through the use of gold or other metal clusters on the membrane.

Though important in its own right, the anodization of cerium to form cerium oxide may be dwarfed by utilizing the same principles to apply a protective anodization layer to iron or steel. Just as we discovered that we could control reaction conditions to create cerium oxide that does not exfoliate from the underlying metal, we have preliminary research that indicates that iron can be polymerized utilizing phosphoric acid. In addition to phosphoric acid, iron has the potential to be polymerized with a variety of organic molecules including oxalate, and poly vinyl alcohol. This research must be followed up as it could lead to a great boon to society.

## 5.2 Cerium Oxide Nanorods

While cerium oxide nanorods show greatly improved catalytic activity over bulk cerium oxide, there is still much to be learned about the effect of defects on catalytic activity. New ways of introducing defect points into the ceria need to be explored towards the end of developing designer catalysts. These defects may be introduced through further refining of the low pressure calcination process. Or more likely, these defects will be produced through the introduction of other metals into the matrix. These metals may be other rare earth compounds, or they may be noble metals. In the case of other rare earth compounds the introduction of atoms into the lattice that are of a greatly different size than the cerium will cause strain. This strain should affect the lattice in a very predictable manner. The strain should be directly proportional to the atomic radius of the dopant atoms, and to the atomic percentage of the dopant atoms. Hypothetically a periodic trend will emerge that will hold true for any monovalent rare earth or transition metal atom. As the majority of rare earth metals are monovalent this should lead to a clear picture of the trend, though violations of any trend are expected and hoped for as

they present opportunities to test previously formed hypothesis and mechanisms. Additionally the periodic trend should lead us closer to understanding the role of multivalency in dopant atoms.

Once the periodic trend is established, the interaction of multiple dopants in the lattice of the cerium oxide should be addressed. Binary dopants will lead to a better understanding of the principles of lattice growth and crystal design. By observing the clustering effects of the dopants the interatomic interactions will become clearer.

Finally it is well accepted that gold clusters below 5nm in size are much more catalytically active than bulk gold.[93] It is therefore possible to hypothesize that very small gold clusters ranging from a single atom to a cluster less than 1 nm will have very good activity. It has been calculated that gold tends to wet the surface of ceria, and form very small clusters based on the amount of gold present. Therefore, it is likely that very small atomic percentages of gold will be able to change the catalytic activity of ceria nanorods. It is also possible that less expensive and more abundant metals than gold will have a significant effect on the catalytic activity of the nanorods. Such metals include copper, tin, and nickel.[27, 86, 94-96]

## 5.3 Summary

The research presented in this thesis merely scratches the surface of understanding the principles behind the catalytic properties of cerium oxide. It could easily take a lifetime to understand this material. However within two to three years there will be a much greater understanding of the role of defects caused by adding dopant atoms to the lattice or decorating the surface of the ceria with atoms or clusters of noble metals, transitions metals, alloys, metal oxides or even non-metals. The range of reaction

which can be catalyzed will only be limited by our understanding of the fundamentals of the catalytic mechanism and the changes to the physical, chemical and electronic properties of the catalyst.

# References

1.      Chen G. Z.,  Xu C. X.,  Song X. Y.,  Zhao W.,  Ding Y.,  Sun S. X., Interface Reaction Route to Two Different Kinds of $CeO_2$ Nanotubes. *Inorg Chem* **2008,** *47* (2), 723-728.

2.      Pan C.,  Zhang D.,  Shi L.,  Fang J., Template-Free Synthesis, Controlled Conversion, and CO Oxidation Properties of $CeO_2$ Nanorods, Nanotubes, Nanowires, and Nanocubes. *Eur J Inorg Chem* **2008,** *2008* (15), 2429-2436.

3.      Luo M.-F.,  Ma J.-M.,  Lu J.-Q.,  Song Y.-P.,  Wang Y.-J., High-Surface Area $CuO$-$CeO_2$ Catalysts Prepared by a Surfactant-Templated Method For Low-Temperature CO Oxidation. *J Catal* **2007,** *246* (1), 52-59.

4.      Sun C. W.,  Chen L. Q., Controllable Synthesis of Shuttle-Shaped Ceria and Its Catalytic Properties for CO Oxidation. *Eur J Inorg Chem* **2009,**  (26), 3883-3887.

5.      Zhong L.-S.,  Hu J.-S.,  Cao A.-M.,  Liu Q.,  Song W.-G.,  Wan L.-J., 3D Flowerlike Ceria Micro/Nanocomposite Structure and Its Application for Water Treatment and CO Removal. *Chem Mater* **2007,** *19* (7), 1648-1655.

6.      Bell A. T.,  Gates B. C.,  Ray D., Basic Research Needs: Catalysis for Energy. DOE, Ed. 2007.

7.      Chorkendorf I.,  Niemantsverdriet J. W., *Concepts of Modern Catalysis and Kinetics*. second ed.; Wiley-VCH: 2007; p 435.

8.      White J. M.,  Bercaw J., Opportunities for Catalysis in the 21st Century. DOE, Ed. 2002; p 30.

9.      Ahrens T. J., *Global Earth Physics : A Handbook of Physical Constants*. American Geophysical Union: Washington, D.C., 1995.

10.     Chen G. Z.,  Xu C. X.,  Song X. Y.,  Xu S. L.,  Ding Y.,  Sun S. X., Template-free Synthesis of Single-Crystalline-like $CeO_2$ Hollow Nanocubes. *Cryst Growth Des* **2008,** *8* (12), 4449-4453.

11.     Gonzalez-Rovira L.,  Sanchez-Amaya J. M.,  Lopez-Haro M.,  Del Rio E.,  Hungria A. B.,  Midgley P.,  Calvino J. J.,  Bernal S.,  Botana F. J., Single-Step Process To Prepare $CeO_2$ Nanotubes with Improved Catalytic Activity. *Nano Lett* **2009,** *9* (4), 1395-1400.

12.     Adachi G.,  Imanaka N.,  Kang Z. C., *Binary Rare Earth Oxides*. Kluwer Academic Publishers: Dordrecht ; Boston, 2004; p xiv, 257 p.

13.     Lide D., *CRC Handbook of Chemistry and Physics*. 88 ed.; CRC: 2007.

14.     Trovarelli A., *Catalysis by Ceria and Related Materials*. 1st ed.; Imperial College Press: London, 2002; p 508.

15.     Gupta C. K.,  Krishnamurthy N., *Extractive Metallurgy of Rare Earths*. CRC Press: Boca Raton, Fla., 2005; p xvii, 484 p.

16.     Patnaik P., *Handbook of Inorganic Chemicals*. McGraw-Hill: New York, 2003; p xv, 1086, 1 p.

17.     Tang C. C.,  Bando Y.,  Liu B. D.,  Golberg D., Cerium Oxide Nanotubes Prepared from Cerium Hydroxide Nanotubes. *Adv Mater* **2005,** *17* (24), 3005-3009.

18.     Kuiry S. C.,  Patil S. D.,  Deshpande S.,  Seal S., Spontaneous Self-Assembly of Cerium Oxide Nanoparticles to Nanorods through Supraaggregate Formation. *J Phys Chem B* **2005,** *109* (15), 6936-6939.


19.     Satyanarayana V. N.,  Kuchibhatla T., Hierarchical Assembly of Inorganic Nanostructure Building Blocks to Octahedral Superstructures a True Template-Free Self-Assembly. *Nanotechnology* **2007,** *18* (7), 075303.


20.     Shan W.,  Dong X.,  Ma N.,  Yao S.,  Feng Z., The Synthesis of Three-Dimensional $CeO_2$ and Their Catalytic Activities for CO Oxidation. *Catal Lett* **2009,** *131* (3), 350-355.


21.     Conesa J. C.,  Martinez-Arias A.,  Fernandez-Garcia M.,  Soria J., Surface Structure and Redox Chemistry of Ceria-Containing Automotive Catalytic Systems. *Res Chem Intermed* **2000,** *26* (1), 103-111.


22.     Smil V., Detonator of the Population Explosion. *Nature* **1999,** *400* (6743), 415.


23.     Somorjai G. A., Introduction to Surface Chemistry and Catalysis. 1 ed.; Nature Publishing Group: 1994.


24.     Zhang Y.,  Rogal J.,  Reuter K., Density-Functional Theory Investigation of Oxygen Adsorption at Pd(11N) Vicinal Surfaces (N=3,5,7): Influence of Neighboring Steps. *Phys Rev B* **2006,** *74*, 125414.


25.     Hammer B.,  Nielsen O. H.,  Narskov J. K., Structure Sensitivity in Adsorption: CO Interaction with Stepped and Reconstructed Pt Surfaces. *Catal Lett* **1997,** *46*, 31-35.

26. Campbell C. T., Ultrathin Metal Films and Particles on Oxide Surfaces: Structural, Electronic and Chemisorptive Properties. *Surf Sci Rep* **1997,** *27* (1-3), 1-111.

27. Campbell C. T., Metal Films and Particles On Oxide Surfaces: Structural, Electronic and Chemisorptive Properties. *J Chem Soc, Faraday Trans* **1996,** *92* (9), 1435-1445.

28. Liu Y., Wen C., Guo Y., Liu X., Ren J., Lu G., Wang Y., Mechanism of CO Disproportionation on Reduced Ceria. *ChemCatChem* **2010,** *2* (3), 336-341.

29. Sales B. C., Turner J. E., Maple M. B., Oscillatory Oxidation of CO over Pt, Pd and Ir Catalysts: Theory. *Surf Sci* **1982,** *114*, 381-394.

30. Rogal J., Reuter K., Scheffler M., CO Oxidation at Pd(100): a First-Principles Constrained Thermodynamics Study. *Phys Rev B* **2007,** *75*, 205433.

31. Hendriksen B. L. M., Ackermann M. D., Van Rijn R., Stoltz D., Popa I., Balmes O., Resta A., Wermeille D., Felici R., Ferrer S., Frenkenjoost W. M., The Role of Steps in Surface Catalysis and Reaction Oscillations. *Nature Chem* **2010,** *2*, 730-734.

32. Robinson I. K., Crystal Truncation Rods and Surface Roughness. *Phys Rev B* **1986,** *33*, 3830-3836.

33. Klikovits J., Step-Orientation-Dependent Oxidation: From 1D to 2D Oxides. *Phys Rev Lett* **2008,** *101*, 266104.

34. Taylor H. S., A Theory of the Catalytic Surface. *Proc R Soc London, Ser A* **1925,** *108*, 105-111.

35.    Wagner C., The Formation of Thin Oxide Films on Metals. *Corros Sci* **1973,** *13*, 23-52.

36.    Yates J. T., Surface Chemistry at Metallic Defect Sites. *J Vac Sci Technol, A* **1995,** *13*, 1359-1367.

37.    Esch F.,  Fabris S.,  Zhou L.,  Montini T.,  Africh C.,  Fornasiero P.,  Comelli G., Rosei R., Electron Localization Determines Defect Formation on Ceria Substrates. *Science* **2005,** *309* (5735), 752-755.

38.    Imbihl R.,  Ertl G., Oscillatory Kinetics in Heterogeneous Catalysis. *Chem Rev* **1995,** *95*, 697-733.

39.    Ivanova A. S., Physicochemical and Catalytic Properties of Systems Based on CeO$_2$. *Kinet Catal* **2009,** *50* (6), 797-815.

40.    Reuter K.,  Scheffler M., First-Principles Atomistic Thermodynamics for Oxidation Catalysis: Surface Phase Diagrams and Catalytically Interesting Regions. *Phys Rev Lett* **2003,** *90*, 046103.

41.    Schth F.,  Henry B. E.,  Schmidt L. D., Oscillatory Reactions in Heterogeneous Catalysis. *Adv Catal* **1993,** *39*, 51-127.

42.    Föll V. H. Agglomerate von Zwischengitteratomen (Swirl-Defekte) in Silizium. Ph. D Thesis, Jahrbuch der Akademie der Wissenschaften Göttingen, 1976.

43.    Zhang C. J.,  Michaelides A.,  King D. A.,  Jenkins S. J., Oxygen Vacancy Clusters on Ceria: Decisive Role of Cerium f Electrons. *Phys Rev B* **2009,** *79* (7).

44.     Babu S.,  Thanneeru R.,  Inerbaev T.,  Day R.,  Masunov A. E.,  Schulte A.,  Seal S., Dopant-Mediated Oxygen Vacancy Tuning in Ceria Nanoparticles. *Nanotechnology* **2009,** *20* (8).

45.     Ganduglia-Pirovano M. V.,  Hofmann A.,  Sauer J., Oxygen Vacancies in Transition Metal And Rare Earth Oxides: Current State of Understanding and Remaining Challenges. *Surf Sci Rep* **2007,** *62* (6), 219-270.

46.     Nolan M.,  Fearon J. E.,  Watson G. W., Oxygen Vacancy Formation and Migration in Ceria. *Solid State Ionics* **2006,** *177* (35-36), 3069-3074.

47.     Fornasiero P.,  Dimonte R.,  Rao G. R.,  Kaspar J.,  Meriani S.,  Trovarelli A., Graziani M., Rh-Loaded $CeO_2$-$ZrO_2$ Solid-Solutions as Highly Efficient Oxygen Exchangers: Dependence of the Reduction Behavior and the Oxygen Storage Capacity on the Structural-Properties. *J Catal* **1995,** *151* (1), 168-177.

48.     Romeo M.,  Bak K.,  Fallah J. E.,  Normand F. L.,  Hilaire L., XPS Study of the Reduction of Cerium Dioxide. *Surf Interface Anal* **1993,** *20* (6), 508-512.

49.     Grabow L.,  Xu Y.,  Mavrikakis M., Lattice Strain Effects on CO Oxidation on Pt(111). *PCCP* **2006,** *8* (29), 3369-3374.

50.     Greeley J.,  Krekelberg W. P.,  Mavrikakis M., Strain-Induced Formation of Subsurface Species in Transition Metals. *Angew Chem Int Ed* **2004,** *43* (33), 4296-4300.

51.     Mavrikakis M.,  Hammer B.,  Nørskov J. K., Effect of Strain on the Reactivity of Metal Surfaces. *Phys Rev Lett* **1998,** *81* (13), 2819.

52.     Vang R. T., Controlling the Catalytic Bond-breaking Selectivity of Ni Surfaces by Step Blocking. *Nat Mater* **2005,** *4*, 160-162.


53.     Hendriksen B. L. M.,  Bobaru S. C.,  Frenken J. W. M., Bistability and Oscillations in CO Oxidation Studied with Scanning Tunneling Microscopy Inside a Reactor. *Catal Today* **2005,** *105*, 234-243.


54.     Martinez-Arias A.,  Conesa J. C.,  Soria J., O2-Probe EPR as a Method for Characterization of Surface Oxygen Vacancies in Ceria-Based Catalysts. *Res Chem Intermed* **2007,** *33* (8-9), 775-791.


55.     Campbell C. T.,  Peden C. H. F., Chemistry - Oxygen Vacancies and Catalysis on Ceria Surfaces. *Science* **2005,** *309* (5735), 713-714.


56.     Sayle T. X. T.,  Parker S. C.,  Catlow C. R. A., The Role of Oxygen Vacancies on Ceria Surfaces in the Oxidation of Carbon Monoxide. *Surf Sci* **1994,** *316* (3), 329-336.


57.     Feynman R., There's Plenty of Room at the Bottom. *Eng Sci* **1960,** *23*, 22-36.


58.     Leapman R. D., Nanoparticles: Dissected with Electrons. *Nat Nanotechnol* **2010,** *5* (7), 480-481.


59.     Mars P.,  Van Krevelen D. W., Oxidation Carried Out by Means of Vanadium Oxide Catalysts. *Spec Suppl Chem Eng Sci* **1954,** *3*, 41-57.


60.     Geerlings J. J. C., Fischer Tropsch Technology from Active Site to Commercial Process. *Appl Catal, A* **1999,** *186*, 27-40.

61.     Zambelli T.,  Wintterlin J.,  Trost J.,  Ertl G., Identification of The Active Sites of a Surface-Catalyzed Reaction.  *Science* **1996,** *273*, 1688-1690.

62.     Williams E. D.,  Bartelt N. C., Thermodynamics of Surface Morphology.  *Science* **1991,** *251*, 393-400.

63.     Park S. D.,  Vohs J. M.,  Gorte R. J., Direct Oxidation of Hydrocarbons in a Solid-Oxide Fuel Cell.  *Nature* **2000,** *404* (6775), 265-267.

64.     Deluga G. A.,  Salge J. R.,  Schmidt L. D.,  Verykios X. E., Renewable Hydrogen from Ethanol by Autothermal Reforming.  *Science* **2004,** *303* (5660), 993-997.

65.     Spiegel C. S., *Designing and Building Fuel Cells*. 1st ed.; McGraw Hill: New York, 2007.

66.     Erbil H. Y.,  Cansoy C. E., Range of Applicability of the Wenzel and Cassie Baxter Equations for Superhydrophobic Surfaces.  *Langmuir* **2009,** *25* (24), 14135-14145.

67.     Yoshimitsu Z.,  Nakajima A.,  Watanabe T.,  Hashimoto K., Effects of Surface Structure on the Hydrophobicity and Sliding Behavior of Water Droplets.  *Langmuir* **2002,** *18* (15), 5818-5822.

68.     Rasband W. S., US NIH http://rsb.info.nih.gov/ij/.

69.     Chen G.,  Sun S.,  Sun X.,  Fan W.,  You T., Formation of Nanotubes from $Ce(OH)CO_3$ Nanorods through Kirkendall Diffusion.  *Inorg Chem* **2009,** *48* (4), 1334-1338.

70.     Fan H. J.,  Gösele U.,  Zacharias M., Formation of Nanotubes and Hollow Nanoparticles Based on Kirkendall and Diffusion Processes: A Review. *Small* **2007,** *3* (10), 1660-1671.

71.     Zhou K.,  Yang Z.,  Yang S., Highly Reducible $CeO_2$ Nanotubes. *Chem Mater* **2007,** *19* (6), 1215-1217.

72.     Thostrup P., Adsorption-induced Step Formation. *Phys Rev Lett* **2001,** *87*, 126102.

73.     Frank F. C., The Influence of Dislocations on Crystal Growth. *Farad Disc* **1949,** *5*, 48-54.

74.     Morin S. A.,  Bierman M. J.,  Tong J.,  Jin S., Mechanism and Kinetics of Spontaneous Nanotube Growth Driven by Screw Dislocations. *Science* **2010,** *328* (5977), 476-480.

75.     Burton W. K.,  Cabrera N.,  Frank F. C., The Growth of Crystals and the Equilibrium Structure of their Surfaces. *Philos Trans R Soc London, Ser A* **1951,** *243* (866), 299-358.

76.     Brunauer S.,  Emmett P. H.,  Teller E., Adsorption of Gases in Multimolecular Layers. *J Am Chem Soc* **1938,** *60*, 309-319.

77.     Kwok R. W. M. *XPSPEAK V. 4.1 XPS Peak Fitting Program for WIN95/98*, Department of Chemistry, The Chinese University of Hong Kong: 1999.

78.	Deshpande S., Patil S., Kuchibhatla S., Seal S., Size Dependency Variation in Lattice Parameter and Valency States in Nanocrystalline Cerium Oxide. *Appl Phys Lett* **2005,** *87* (13), 3.

79.	Holgado J. P., Alvarez R., Munuera G., Study of $CeO_2$ XPS Spectra by Factor Analysis: Reduction of $CeO_2$. *Appl Surf Sci* **2000,** *161* (3-4), 301-315.

80.	Mullins D. R., Overbury S. H., Huntley D. R., Electron Spectroscopy of Single Crystal and Polycrystalline Cerium Oxide Surfaces. *Surf Sci* **1998,** *409* (2), 307-319.

81.	Paparazzo E., Ingo G. M., Zacchetti N., X-Ray Induced Reduction Effects at $CeO_2$ Surfaces: An X-Ray Photoelectron Spectroscopy Study. *J Vac Sci Technol, Part A* **1991,** *9* (3), 1416-1420.

82.	Stierle A., A Surface X-Ray Study of The Structure And Morphology of the Oxidized Pd(001) Surface. *J Chem Phys* **2005,** *122*, 044706.

83.	Paparazzo E., XPS Studies of Damage Induced by X-Ray Irradiation On $CeO_2$ Surfaces. *Surf Sci* **1990,** *234* (1-2), L253-L258.

84.	Dahl S., Role of steps in $N_2$ activation on Ru(0001). *Phys Rev Lett* **1999,** *83*, 1814-1817.

85.	Kim C. H., Qi G., Dahlberg K., Li W., Strontium-Doped Perovskites Rival Platinum Catalysts for Treating $NO_x$ in Simulated Diesel Exhaust. *Science* **2010,** *327* (5973), 1624-1627.

86.	Spenadel L., Boudart M., Dispersion of Platinum on Supported Catalysts. *J Phys Chem A* **1960,** *64* (2), 204-207.

87.     Otsuka K.,  Ushiyama T.,  Yamanaka I., Partial Oxidation of Methane Using the
Redox of Cerium Oxide
 *Chem Lett* **1993,**  (9), 1517-1520.


88.     Hendriksen B. L. M.,  Bobaru S. C.,  Frenken J. W. M., Oscillatory CO oxidation
on Pd(100) studied with in situ scanning tunneling microscopy.  *Surf Sci* **2004,** *552*, 229-
242.


89.     Ackermann M. D., Structure and reactivity of surface oxides on Pt(110) during
catalytic CO oxidation.  *Phys Rev Lett* **2005,** *95*, 255505.


90.     Lundgren E., Kinetic Hindrance During the Initial Oxidation Of Pd(100) at
Ambient Pressures.  *Phys Rev Lett* **2004,** *92*, 046101.


91.     Hendriksen B. L. M.,  Frenken J. W. M., CO Oxidation on Pt(110): Scanning
Tunneling Microscopy Inside a Flow Reactor.  *Phys Rev Lett* **2002,** *89*, 046101.


92.     Boudart M., Turnover Rates in Heterogeneous Catalysis.  *Chem Rev* **1995,** *95* (3),
661-666.


93.     Akita T.,  Okumura M.,  Tanaka K.,  Kohyama M.,  Haruta M., TEM observation
of gold nanoparticles deposited on cerium oxide.  *J Mater Sci* **2005,** *40* (12), 3101-3106.


94.     Zhou G. W., Metal-Oxide Interfaces at the Nanoscale.  *Appl Phys Lett* **2009,** *94*
(23).


95.     Martinez N. D.,  Venturini R. B.,  Silva H. S.,  Gonzalez J. E.,  Rodriguez A. M.,
Copper on Activated Carbon for Catalytic Wet Air Oxidation.  *Mater Res Ibero American
J Mater* **2009,** *12* (1), 45-50.

96.    Gao F., Wang Y., Cai Y., Goodman D. W., CO Oxidation on Pt-Group Metals from Ultrahigh Vacuum to Near Atmospheric Pressures. Part 2. Palladium and Platinum. *J Phys Chem C* **2009,** *113*, 174-181.